Development of Ti-Mo-Fe alloys combining different plastic deformation mechanisms for improved strength-ductility trade-off and high work hardening rate

Journal of Alloys and Compounds

Development of Ti-Mo-Fe alloys combining different plastic deformation mechanisms for improved strength-ductility trade-off and high work hardening rate

--Manuscript Draft--

Manuscript Number:	
Article Type:	Full Length Article
Keywords:	Titanium alloy; Mechanical twinning; Stress-induced martensitic transformation; Stress relaxation mechanism; Precipitates/twin interactions
Corresponding Author:	Diego Mantovani Laval University Quebec, PQ CANADA
First Author:	Carolina Catanio Bortolan
Order of Authors:	Carolina Catanio Bortolan
	Leonardo Contri Campanelli
	Paolo Mengucci
	Gianni Barucca
	Nicolas Giguère
	Nicolas Brodusch
	Carlo Paternoster
	Claudemiro Bolfarini
	Raynald Gauvin
	Diego Mantovani
Abstract:	Titanium-based biomaterials are the gold standard for orthopedic implants; however, they are not generally suitable for the manufacture of intravascular stents. Their low strength-ductility trade-off and low work hardening rate are their main limitations. However, Ni-free alloys are desirable for such application in order to avoid allergic reactions caused by the high-Ni content materials applied nowadays. Therefore, in this study, three alloys of the Ti-Mo-Fe system (Ti-8Mo-2Fe, Ti-9Mo-1Fe and Ti-10.5Mo-1Fe) were designed to exhibit high strength-ductility compromise and high work hardening rate. Their microstructures, mechanical properties and plastic deformation mechanism were investigated. Athermal ω precipitates were observed in the β matrix of all solution-treated alloys. In the solution-treated β matrix of Ti-9Mo-1Fe alloy, additional nanometer-sized α" particles were found by transmission electron microscopy (TEM). Although combined TWIP/TRIP effects were expected by the design method in the Ti-8Mo-2Fe and Ti-9Mo-1Fe alloys, no TRIP effect was observed. In fact, stress-induced martensitic (SIM) transformation occurred mainly at the {332}<113> twins/matrix interfaces for all the deformed microstructures, including Ti-10.5Mo-1Fe alloy, and it acted as a localized stress-relaxation mechanism, delaying the fracture. Based on the electron backscatter diffraction (EBSD) analyses, in Ti-8Mo-2Fe and Ti-10.5Mo-1Fe alloys, the formation of a dense network of {332}<113> twins was the responsible for their high and steady work hardening rates (1370 and 1120 MPa) and large uniform elongations (22 and 34%). The absence of SIM α" as a primary plastic deformation mechanism and the solid solution hardening of Fe resulted in their high strengths (yield strength of 772 and 523 MPa). In Ti-9Mo-1Fe, the formation of mechanical twinning was hindered, resulting in limited strain-hardening capability and in a low uniform elongation (6%). It is thought that the nanometer-sized α" particles in its β matrix in conjunction with athermal ω precipitates detrimentally affected mechanical twinning and the ductility of this alloy.
Suggested Reviewers:	Geetha Manivasagam Professor, VIT University geethamanivasagam@vit.ac.in Professor Manivasagam has an expertise on Ti-alloys, physical metallurgy of Beta Ti

	alloys, medical applications, ductility.
	Beto Grandini Professor, Sao Paulo State University Julio de Mesquita Filho betog@fc.unesp.br Professor Grandini has an expertise on Ti-alloys, metallurgy, biomaterials, design, processes.
	Minjie Lai Early career scientist, Max-Planck-Institute Germany m.lai@mpie.de Dr. Lai has an expertise on Ti-alloys and more specifically on deformation mechanisms of beta Ti-alloys.
	Ivan Gutierrez-Urrutia Senior Researcher, National Institute for Materials Science gutierrezurrutia.Ivan@nims.go.jp Gutierrez-Urrutia has expertise on deformation mechanisms of both Ti-alloys and steels.
Opposed Reviewers:	Frédéric Prima Professor, Chimie ParisTech, France frederic.prima@chimieparistech.psl.eu Professor Prima is a scientist in potential conflict of interest. There has been some conflicts between us in previous collaborations.
	Fan Sun Chimie ParisTech, France fan.sun@chimieparistech.psl.eu Dr. Sun is a scientist in potential conflict of interest. There has been some conflicts between us in previous collaborations.
	Thierry Gloriant Professor, University of Rennes, France Thierry.Gloriant@insa-rennes.fr Professor Gloriant is a scientist in potential conflict of interest. There has been some conflicts between us in previous collaborations.
	Pascal Jacques Université Catholique de Louvain, Belgium pascal.jacques@uclouvain.be Professor Jacques is a scientist in potential conflict of interest. There has been some conflicts between us in previous collaborations.
Order of Authors:	Carolina Catanio Bortolan
	Leonardo Contri Campanelli
	Paolo Mengucci
	Gianni Barucca
	Nicolas Giguère
	Nicolas Brodusch
	Carlo Paternoster
	Claudemiro Bolfarini
	Raynald Gauvin
	Diego Mantovani

UNIVERSITÉ LAVAL

Canada Research Chair in Biomaterials and Bioengineering for the Innovation in Surgery
Laboratory for Biomaterials and Bioengineering
School of Science and Engineering

Quebec City, June 24 2022

Professor V. Pecharsky
Editor of the Journal of Alloys and Compounds
Professor, Iowa State University
Department of Materials Science and Engineering
Ames, IA 50011, United States of America

Dear Professor Pecharsky,

The use of new metallic materials in medical applications has risen exponentially in recent years. This usage is particularly relevant in medicine, where applications range from the treatment of early stage disease to implants for major trauma. There may be demand for a research work introducing alloys by designing specific to medical applications. This manuscript introduces new Ti-alloys with twinning properties. In fact, although Ti alloys have been largely investigated, the TRIP/TWIP zone of the phase diagram is rather imprecise and undefined, and need further investigation. This has the potential to shed new lights in the family of Ti alloys and their broad applications, including non-medical such as automotive, aerospace and others. To our opinion, this might be of high interest for the readers of Journal of Alloys and Compounds.

Our group at Laval University has been working closely with other research institutions, particularly the Federal University of São Carlos, in Brazil, Polytechnic of the Marche, in Italy, and McGill University, here in Canada, as well as the Technological Development Centre in Trois-Rivières, Canada. This has brought together a group that has a track-record in developing novel biomaterials and another with know-how to assess and rapidly translate new findings into advanced metallic alloys. A close collaboration between our institutes raised twinning-induced plasticity (TWIP)/transformation-induced plasticity (TRIP) β-titanium alloys.

We believe that we are on the verge of a paradigm shift that will open the doors for new generation of implant devices, which deserves the attention of the readers of Journal of Alloys and Compounds. We would value the opportunity to share our perspective with the community, and we would like to submit an original manuscript

Pavillon Adrien-Pouliot, 1745E
1065, avenue de la Médecine
Québec (Québec) G1V 0A6
CANADA

+1 418 656-2131 poste 6270
Télécopieur : + 1 418 656-5343
Diego.Mantovani@gmn.ulaval.ca
www.lbb.ulaval.ca ; www.iBiomat.ulaval.ca

UNIVERSITÉ LAVAL

Canada Research Chair in Biomaterials and Bioengineering for the Innovation in Surgery
Laboratory for Biomaterials and Bioengineering
School of Science and Engineering

entitled "*Development of Ti-Mo-Fe alloys combining different plastic deformation mechanisms for improved strength-ductility trade-off and high work hardening rate*" for a section of your esteemed journal "Journal of Alloys and Compounds".

Although several β-Ti alloys combining TWIP/TRIP effects have been investigated in the past ten years, stress-induced martensitic transformation was shown to occur in the designed alloys not as a primary deformation mechanism, but as a stress-relaxation mechanism. Moreover, for one of the three designed Ti-Mo-Fe alloys, the co-existence of nanometer-sized martensitic α" and athermal ω precipitates prior to deformation was suggested to hinder mechanical twinning, resulting in limited work hardening capability and ductility.

I am convinced that the novel elucidations of the effect of martensite (quenched and stress-induced) in TWIP Ti-based alloys can be of great interest to a variety of audiences, from metallurgists to biomaterials scientists and manufacturing engineers.

This manuscript has not been published and it is not under consideration for publication elsewhere. We have no conflicts of interest to disclose.

We look forward to hearing from you.

Diego Mantovani

Professor Diego Mantovani
Director of Laboratory for Biomaterials and Bioengineering
Dept of Min-Met-Materials Engineering, Laval University

On behalf of all co-authors:
Carolina Catanio Bortolan – carolina.catanio-bortolan.1@ulaval.ca
Leonardo Contri Campanelli – leonardo.campanelli@unifesp.br
Paolo Mengucci – p.mengucci@staff.univpm.it
Gianni Barucca – g.barucca@staff.univpm.it
Nicolas Giguère – nicolas.giguere@cegeptr.qc.ca
Nicolas Brodusch – nicolas.brodusch@mcgill.ca
Carlo Paternoster – carlo.paternoster.1@ulaval.ca
Claudemiro Bolfarini – cbolfa@ufscar.br
Raynald Gauvin – raynald.gauvin@mcgill.ca

Pavillon Adrien-Pouliot, 1745E
1065, avenue de la Médecine
Québec (Québec) G1V 0A6
CANADA

+1 418 656-2131 poste 6270
Télécopieur : + 1 418 656-5343
Diego.Mantovani@gmn.ulaval.ca
www.lbb.ulaval.ca ; www.iBiomat.ulaval.ca

UNIVERSITÉ LAVAL

Canada Research Chair in Biomaterials and Bioengineering for the Innovation in Surgery
Laboratory for Biomaterials and Bioengineering
School of Science and Engineering

Quebec City, June 24 2022

Prime Novelty Statement,

(1) This manuscript is the authors' original work. It has not been published and it is not under consideration for publication elsewhere;
(2) All the authors have checked the manuscript and have agreed to the submission.

Professor Diego Mantovani (Corresponding Author)
Director of Laboratory for Biomaterials and Bioengineering
Dept of Min-Met-Materials Engineering, Laval University

On behalf of all co-authors:
Carolina Catanio Bortolan – carolina.catanio-bortolan.1@ulaval.ca
Leonardo Contri Campanelli – leonardo.campanelli@unifesp.br
Paolo Mengucci – p.mengucci@staff.univpm.it
Gianni Barucca – g.barucca@staff.univpm.it
Nicolas Giguère – nicolas.giguere@cegeptr.qc.ca
Nicolas Brodusch – nicolas.brodusch@mcgill.ca
Carlo Paternoster – carlo.paternoster.1@ulaval.ca
Claudemiro Bolfarini – cbolfa@ufscar.br
Raynald Gauvin – raynald.gauvin@mcgill.ca

Pavillon Adrien-Pouliot, 1745E
1065, avenue de la Médecine
Québec (Québec) G1V 0A6
CANADA

+1 418 656-2131 poste 6270
Télécopieur : + 1 418 656-5343
Diego.Mantovani@gmn.ulaval.ca
www.lbb.ulaval.ca ; www.iBiomat.ulaval.ca

Development of Ti-Mo-Fe alloys combining different plastic deformation mechanisms for improved strength-ductility trade-off and high work hardening rate

Carolina Catanio Bortolan[a], Leonardo Contri Campanelli[b], Paolo Mengucci[c], Gianni Barucca[c], Nicolas Giguère[d], Nicolas Brodusch[e], Carlo Paternoster[a], Claudemiro Bolfarini[f], Raynald Gauvin[e], Diego Mantovani[a, *]

Affiliation:

[a]: *Laboratory for Biomaterials and Bioengineering (LBB). Canada Research Chair Tier I in Biomaterials and Bioengineering for the Innovation in Surgery, Department of Mining, Metallurgy, and Materials Engineering, Laval University, Quebec City, G1V 0A6, Canada*

[b]: *Institute of Science and Technology (ICT), Federal University of São Paulo – UNIFESP, São José dos Campos, 12231-280, Brazil*

[c]: *Dipartimento di Scienze e Ingegneria della Materia dell'Ambiente ed Urbanistica – SIMAU, Università Politecnica delle Marche, Ancona, 60131, Italy*

[d]: *Quebec Metallurgy Center (CMQ), Trois-Rivières, G9A 5E1, Canada*

[e]: *Department of Mining and Materials Engineering, McGill University, Montreal, H3A 0C5, Canada*

[f]: *Department of Materials Engineering (DEMa), Federal University of São Carlos – UFSCar, São Carlos, 13565-905, Brazil*

***Corresponding Author:**

Prof. Diego Mantovani

Laboratory for Biomaterials and Bioengineering, Canada Research Chair Tier 1 in Biomaterials and Bioengineering for the Innovation in Surgery

Department Mining, Metallurgy, and Materials – Laval University

Pavilion Adrien-Pouliot, Local 1745-E

Telephone: +1-418-656-2131

Email: Diego.Mantovani@gmn.ulaval.ca

Abstract:

Titanium-based biomaterials are the gold standard for orthopedic implants; however, they are not generally suitable for the manufacture of intravascular stents. Their low strength-ductility trade-off and low work hardening rate are their main limitations. However, Ni-free alloys are desirable for such application in order to avoid allergic reactions caused by the high-Ni content materials applied nowadays. Therefore, in this study, three alloys of the Ti-Mo-Fe system (Ti-8Mo-2Fe, Ti-9Mo-1Fe and Ti-10.5Mo-1Fe) were designed to exhibit high strength-ductility compromise and high work hardening rate. Their microstructures, mechanical properties and plastic deformation mechanism were investigated. Athermal ω precipitates were observed in the β matrix of all solution-treated alloys. In the solution-treated β matrix of Ti-9Mo-1Fe alloy, additional nanometer-sized α" particles were found by transmission electron microscopy (TEM). Although combined TWIP/TRIP effects were expected by the design method in the Ti-8Mo-2Fe and Ti-9Mo-1Fe alloys, no TRIP effect was observed. In fact, stress-induced martensitic (SIM) transformation occurred mainly at the {332}<113> twins/matrix interfaces for all the deformed microstructures, including Ti-10.5Mo-1Fe alloy, and it acted as a localized stress-relaxation mechanism, delaying the fracture. Based on the electron backscatter diffraction (EBSD) analyses, in Ti-8Mo-2Fe and Ti-10.5Mo-1Fe alloys, the formation of a dense network of {332}<113> twins was the responsible for their high and steady work hardening rates (1370 and 1120 MPa) and large uniform elongations (22 and 34%). The absence of SIM α" as a primary plastic deformation mechanism and the solid solution hardening of Fe resulted in their high strengths (yield strength of 772 and 523 MPa). In Ti-9Mo-1Fe, the formation of mechanical twinning was hindered, resulting in limited strain-hardening capability and in a low uniform elongation (6%). It is thought that the

nanometer-sized α" particles in its β matrix in conjunction with athermal ω precipitates detrimentally affected mechanical twinning and the ductility of this alloy.

Keywords: Titanium alloy, Mechanical twinning, Stress-induced martensitic transformation, Stress relaxation mechanism, Precipitates/twin interactions

1. Introduction

Titanium alloys have been widely applied in the biomedical and aerospace fields. The main characteristics making these metals attractive to be used as biomaterials are their high strength to density ratio, their high biocompatibility, especially for dental and orthopedic applications, their high corrosion resistance [1], and the possibility to design alloys without recognized toxic, allergenic and carcinogenic elements such as Ni [1-3]. It is mainly this last advantage and the rising prevalence of Ni allergy in the population [4] that are motivating researchers to develop new Ti alloys for the production of vascular stents [5-11]. In fact, the currently most applied materials to fabricate these devices, 316L stainless steel (Fe-18Cr-14Ni-2.5Mo, wt.%), nitinol (55Ni-45Ti) and Co-Cr alloys such as L605 (Co-20Cr-15W-10Ni), contain a high amount of Ni [12]. Although controversial, it seems that the release of Ni ions from these metallic devices can also increase the risk of in-stent restenosis (ISR) [12], a cause of stent failure consisting in the formation of a new atherosclerotic plaque in the region of the implanted stent [13].

Ti alloys show some disadvantages for this kind of applications, that is an insufficient radiopacity in thin structures [14], low strength-ductility trade-off [7, 15], low elastic modulus [5] and insufficient recoverable strain [16]. In particular, low elastic modulus is not acceptable for balloon-expandable stents [5], while self-expandable stents require a relevant recoverable strain [16]. The works that have been performed to overcome these limitations follow mainly two different strategies. One of them, for fabrication of balloon-expandable stents, consists in the development of alloys with high elastic modulus in order to reduce elastic recoil after the deployment of the device inside vessels [5, 6]. The other one, for the manufacture of self-expandable stents, is focused on the development of superelastic alloys with improved recoverable strain [7, 9, 10, 17, 18].

In addition to these strategies, the development of β Ti alloys with high strength-ductility trade-off and high work hardening rate, resultant from the combination of twinning-induced plasticity (TWIP) and transformation-induced plasticity (TRIP) effects, has been explored [19, 20]. Ti-12Mo (wt.%) was the first designed and produced Ti alloy belonging to the TWIP/TRIP family [21, 22]. It exhibits a high work hardening rate of around 2000 MPa [23], a high ductility with total elongation of 45%, and a *relatively* high ultimate tensile strength (UTS) of 660 MPa [24]. The word "*relatively*" was used in the previous sentence because its UTS is still low when compared to L605 (UTS of 950 - 1200 MPa [15]), the reference alloy in terms of required mechanical properties for balloon-expandable stents. The highest UTS is desired to allow the production of stents with thinner wall thickness for improved flexibility, deliverability [15, 16] and clinical outcomes [25, 26]. Besides TWIP/TRIP Ti-based alloys, the combination of twinning and dislocation slip as plastic deformation mechanisms in Ti-Mo alloys was also reported to lead to improved strength-ductility compromise [27].

The purpose of the present study was to develop new Ti-Mo-Fe alloys with high strength-ductility trade-off and high work hardening rate as potential candidates for the manufacture of vascular stents. To achieve this, the chemical compositions were designed to have, in one side, alloys combining TWIP and TRIP effects, and, on another side, an alloy combining twinning and dislocation slip as plastic deformation mechanisms. Fe was selected as the second alloying element, mainly because it is one of the most effective solid solution strengthening β stabilizer [28], thus improvements in terms of strength are expected in comparison to Ti-12Mo alloy. Moreover, it is the cheapest β stabilizer [29], with strong β stabilization capacity [30], and it is, in general, considered as non-toxic for humans [31]. Besides the investigation of microstructural characteristics and of mechanical properties, the plastic deformation mechanisms of these Ti-Mo-Fe alloys

were studied in order to validate the effectiveness of the strategy to design TWIP/TRIP Ti alloys [21, 22, 32], described in the subsequent section, for this ternary system.

2. Materials and methods

2.1. Compositional design

Prima and coworkers [21, 22, 32] proposed a semi-empirical approach to design TWIP/TRIP Ti alloys for improved strength-ductility trade-off and strain hardening. In this approach, the chemical stability of the β phase, indicated by two electronic parameters, $\overline{Bo}$ (bond order) and $\overline{Md}$ (mean d-orbital energy level), was related to the occurrence of plastic deformation mechanisms, such as dislocation slip, mechanical twinning and stress-induced transformation [22]. Details about the theory and calculations behind these electronic parameters can be found elsewhere [33, 34]. The researchers proposed a general $\overline{Bo}$ - $\overline{Md}$ map [32], as can it be seen in Fig. 1, in which a new transition line was added, M_d = RT (room temperature). In fact, the M_d line corresponds to the transition between the mechanical twinning and stress-induced transformation deformation modes. For optimized combination of TWIP and TRIP effects, the designed alloy should be situated around this line [22, 32]. The primary transition line already existing (slip/twin) separates the alloys deforming mainly by dislocation slip and mechanical twinning.

Using this approach as a guiding tool, in the present study two compositions, Ti-8Mo-2Fe ($\overline{Bo} = 2.7989$ and $\overline{Md} = 2.4002$) and Ti-9Mo-1Fe ($\overline{Bo} = 2.8016$ and $\overline{Md} = 2.4108$) in wt.%, were selected as potential candidates to combine TWIP/TRIP effects since they are situated around the M_d line as shown in Fig. 1. Besides these compositions, Ti-10.5Mo-1Fe alloy ($\overline{Bo} = 2.8038$ and $\overline{Md} = 2.4066$) was selected as a potential

candidate to combine mechanical twinning and dislocation slip as plastic deformation mechanisms, since it is located around the transition pure slip/twin line.

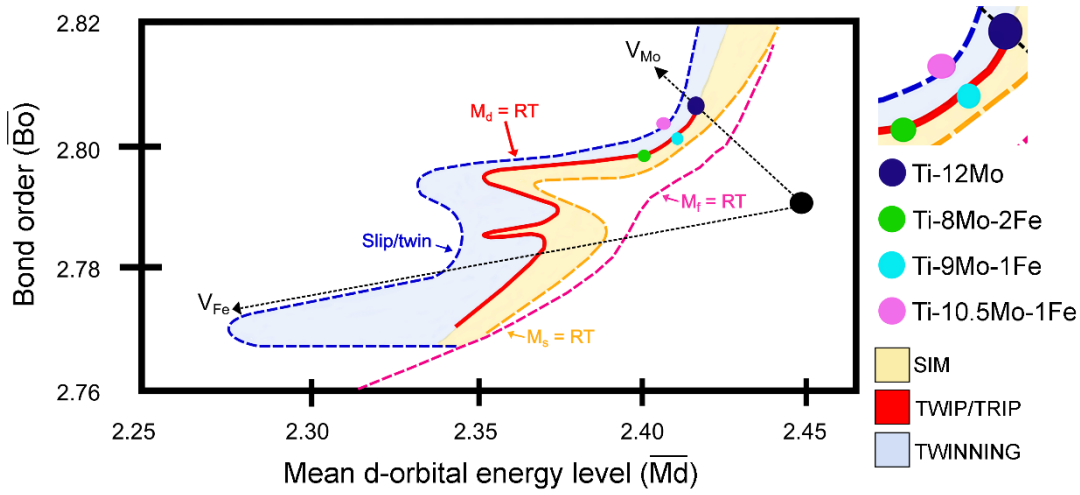

Fig. 1. $\overline{Bo}$ - $\overline{Md}$ diagram showing the position of Ti-8Mo-2Fe, Ti-9Mo-1Fe and Ti-10.5Mo-1Fe alloys. Adapted with permission from ref. [32].

2.2. Materials preparation

Cylindrical Ti-8Mo-2Fe, Ti-9Mo-1Fe and Ti-10.5Mo-1Fe (wt.%) alloy ingots (diameter Ø = 50 mm and length L = 250 mm) were produced from pure metals in an induction vacuum furnace (Consarc, USA) under the protection of a high-purity argon atmosphere. Grade 2 pure titanium bars with a maximum oxygen content of 0.07 wt.% (Titanium Industries Inc., Canada), Mo with 99.85% purity (Titanium Industries Inc., Canada) and Fe with 99.9% purity (Allied Metals, USA) were used as raw materials, in order to achieve low oxygen content alloys. The ingots were hot isostatically pressed at 140 MPa for 2 h at 900 °C in a HP1030 press (American Isostatic Presses Inc., USA), in order to remove shrinkage and porosity coming from casting. They were machined to Ø = 33 mm diameter ingots and then rotary swaged at 900 °C under ambient atmosphere conditions, with a cross-sectional area reduction of 75%. This cross-sectional area reduction was gradual, i.e., 5 passes of rotary swaging were performed, each one using a die with a smaller diameter than the previous one. In order to keep the bars at 900 °C, they were

immediately re-heated after each pass. After the swaging procedure, a solution heat treatment was performed at 900 °C for 1 h under Ar atmosphere, followed by water quenching, in order to retain a fully β microstructure at room temperature. The analyzed Mo, Fe and final O content are shown in Table 1. The O content was analyzed by inert gas fusion method (ASTM E1409-13 standard), while Mo and Fe were assessed by inductively coupled plasma atomic emission spectroscopy (ICP-AES) following the ASTM D1976-12 standard.

Table 1. Nominal and analyzed Mo, Fe and O content of the Ti-Mo-Fe alloys (wt. %).

Alloy	Mo	Fe	O
Ti-8Mo-2Fe	7.7 ± 0.1	2.0 ± 0.0	0.05 ± 0.00
Ti-9Mo-1Fe	9.1 ± 0.1	1.1 ± 0.0	0.09 ± 0.00
Ti-10.5Mo-1Fe	10.6 ± 0.1	1.1 ± 0.0	0.05 ± 0.00

2.3. Mechanical characterization

Room temperature tensile tests were performed on cylindrical specimens with gage dimensions of 6 mm diameter and 24 mm length, at a strain rate of 10^{-3} s^{-1} in a SATEC T20000 machine. The tests were carried out using an extensometer and following the ASTM E8 standard. Three specimens for each alloy were tested until failure. Moreover, interrupted tensile tests up to a total strain of 3% were performed on the same alloys, to evaluate their plastic deformation mechanisms.

Their dynamic elastic moduli were measured by an impulse excitation technique. The measurements were performed with a Sonelastic® equipment (ATCP Physical Engineering, Brazil) following the ASTM E1876-15 standard. Details concerning the technique can be found elsewhere [35]. Two cylindrical samples, with a diameter of 12 mm and a length of 60 mm (obtained from the center of the bars along the longitudinal direction) were tested for each alloy; three measurements were performed for each sample. Vickers microhardness measurements were also performed according to the

ASTM E384 standard by employing a 200 gf load during an indent period of 13 s using a Clemex CMT.HD (Clemex, Canada). Ten measurements were done for each alloy.

2.4. Microstructural characterization

Solution-treated alloys (condition label: ST)

Prior to conventional metallographic observations of the solution-treated alloys using a LECO 300 optical microscope (LECO Corporation, USA), the samples were mechanically polished until a mirror surface finishing, and finally etched with Kroll's reagent (100 mL H_2O, 5 mL HNO_3 and 2 mL HF). Grain size analyses were carried out using the grain area determination method from low magnification EBSD maps containing 49 (Ti-8Mo-2Fe), 86 (Ti-9Mo-1Fe) and 77 (Ti-10.5Mo-1Fe) non-border grains. The maps were acquired by a NordlysMax detector (Oxford Instruments, UK) installed on a Hitachi SU-3500 (Hitachi High-Technologies, Japan) scanning electron microscope (SEM), and the data were analyzed using the Channel5 software suite (Oxford Instruments, UK). Prior to EBSD analyses, the polished samples were subjected to broad ion beam milling in a Hitachi IM-4000 Plus instrument under an Ar^+ beam at 4 kV. For phase identification, x-ray diffraction (XRD) was conducted in a Bruker D8 Advance diffractometer (Bruker, Germany) at V = 40 kV and I = 40 mA, with Cu-Kα radiation ($\lambda_{CuK\alpha}$ = 1.5418 Å), and an angular step size 2θ = 0.02°. Peaks were identified by the DIFFRAC.EVA software package (release 2018, Bruker AXS) using the PDF database of the International Centre for Diffraction Data (ICDD). Rietveld analysis was carried out by the MAUD (Material Analysis Using Diffraction, http:/maud.radiophema.com/) software, after calibration of the instrumental broadening by reference Al_2O_3 powder. Lattice parameters were calculated from angular position of the β phase peaks by using the peak analyzer function included in the Origin software package (OriginLab, USA). Furthermore, peak relative intensity was calculated from peak shape analysis of XRD

patterns. The distributions of Mo and Fe in the alloys were mapped by electron-probe microanalysis (EPMA) with a CAMECA SX-100 equipment (CAMECA, France) using a step size of 3 µm.

Alloys after 3% total strain (condition label: 3%)

Deformation microstructures of the interrupted tensile tests were firstly observed in a Nikon Eclipse ME600 optical microscope (Nikon, Japan). Before optical microscopy, the samples were prepared in the same way as described above for the solution-treated alloys. EBSD analyses were performed using a Bruker eFlash EBSD camera (Bruker Gmbh, Germany) fitted on a Hitachi SU-8230 SEM (Hitachi High-Technologies, Japan) with a step size between 0.6 and 0.8 µm. Prior to EBSD, the mechanically polished samples were submitted to broad ion beam milling with a Hitachi IM-3000 flat milling system (Hitachi High-Technologies, Japan) under an Ar^+ beam with an accelerating voltage of 5 kV. The acquired EBSD data were analyzed using both ATEX© software [36] and Channel5 software suite (Oxford Instruments, UK). The density of {332}<113> twins [μm^{-1}] was calculated by dividing the total length of {332}<113> twin boundaries by the scanned area. The total length was calculated by multiplying the number of map-pixels corresponding to such boundaries (obtained using ImageJ software, National Institutes of Health, USA) by the step size in µm. The XRD analyses described above for the solution-treated condition were also performed for the strained alloys.

For finer microstructural observations of both solution-treated and after 3% strain conditions, transmission electron microscopy (TEM) analyses were performed in a Philips CM200 microscope equipped with a LaB_6 filament. TEM samples were prepared using the following procedure: 3 mm-diameter disks were cut from the bulk material by an ultrasonic cutter (Gatan, USA) and polished by using abrasive papers and diamond pastes. In order to reduce time of ion milling, each 3 mm disk was mechanically thinned

in the central area by a Dimple Grinder (Gatan, USA). Final thinning was carried out using a PIPS (Gatan, USA) ion beam system using Ar^+ ions at 5 kV [37].

3. Results

3.1 Microstructural characterization of the alloys in the solution-treated condition

Fig. 2 shows the optical micrographs of (a) Ti-8Mo-2Fe, (b) Ti-9Mo-1Fe and (c) Ti-10.5Mo-1Fe alloys in the solution-treated condition, their grain size distributions obtained from low magnification EBSD maps (Fig. 2 (d-f)) and their XRD patterns (Fig. 2 (g) and (h)). A fully β microstructure with equiaxed and relatively coarse grains was observed for all of them. The average grain size was 230, 176 and 193 μm for Ti-8Mo-2Fe, Ti-9Mo-1Fe and Ti-10.5Mo-1Fe, respectively. All the alloys exhibited a broad grain size distribution (Fig. 2 (d-f)) with a minimum grain size of around 20 μm and maximum ones of around 555 μm (Ti-8Mo-2Fe), 395 μm (Ti-9Mo-1Fe) and 455 μm (Ti-10.5Mo-1Fe). The presence of "stripes" along the longitudinal direction was also observed in the optical micrographs of solution-treated alloys (Fig. 2 (a-c)). They resulted from the solidification segregation of Mo and Fe, which was described below in the EPMA analyses section. Similar results were reported for Ti-15Mo-5Zr, for which the impact of applied thermomechanical processing on the segregation has been put in evidence [38].

The most intense peaks in the XRD patterns of solution-treated alloys, Fig. 2 (g) and (h), were due to cubic (bcc) β phase. From the XRD patterns plotted in square root (SQRT) intensity scale, Fig. 2 (h), low intensity diffraction effects due to the athermal ω phase were evidenced. Rietveld refinement allowed the estimation of ω phase amount (in wt.%) as well as lattice parameters of β and ω phases for each condition. Lattice parameter values and weight fraction of ω phase for alloys in solution-treated condition were summarized in Table 3, where a comparison with the deformed (3% strain) condition was

also offered. The weight fraction of ω phase was similar in the ST Ti-8Mo-2Fe ((35 ± 4) wt.%) and Ti-9Mo-1Fe ((33 ± 2) wt.%) alloys. Solution-treated Ti-10.5Mo-1Fe alloy exhibited the largest fraction of ω phase, that is (45 ± 3) wt.%. Regarding the lattice parameters of ω phase, no difference was observed between ST Ti-8Mo-2Fe and Ti-10.5Mo-1Fe alloys; Ti-9Mo-1Fe showed slightly lower lattice parameters. The lattice parameter of the β phase was lower than the nominal value reported in the 89-4913 ICDD file (a = 3.283 Å) for all the ST alloys. In particular, the lattice parameter of β phase was a = 3.2660 Å, a = 3.2599 Å and a = 3.2643 Å for Ti-8Mo-2Fe, Ti-9Mo-1Fe and Ti-10.5Mo-1Fe, respectively. Regarding texture, a qualitative evaluation from the XRD patterns carried out by comparing the experimental intensity values of β peaks to the nominal ones (ICDD n. 89-4913) evidenced a substantial absence of texture for all ST alloys.

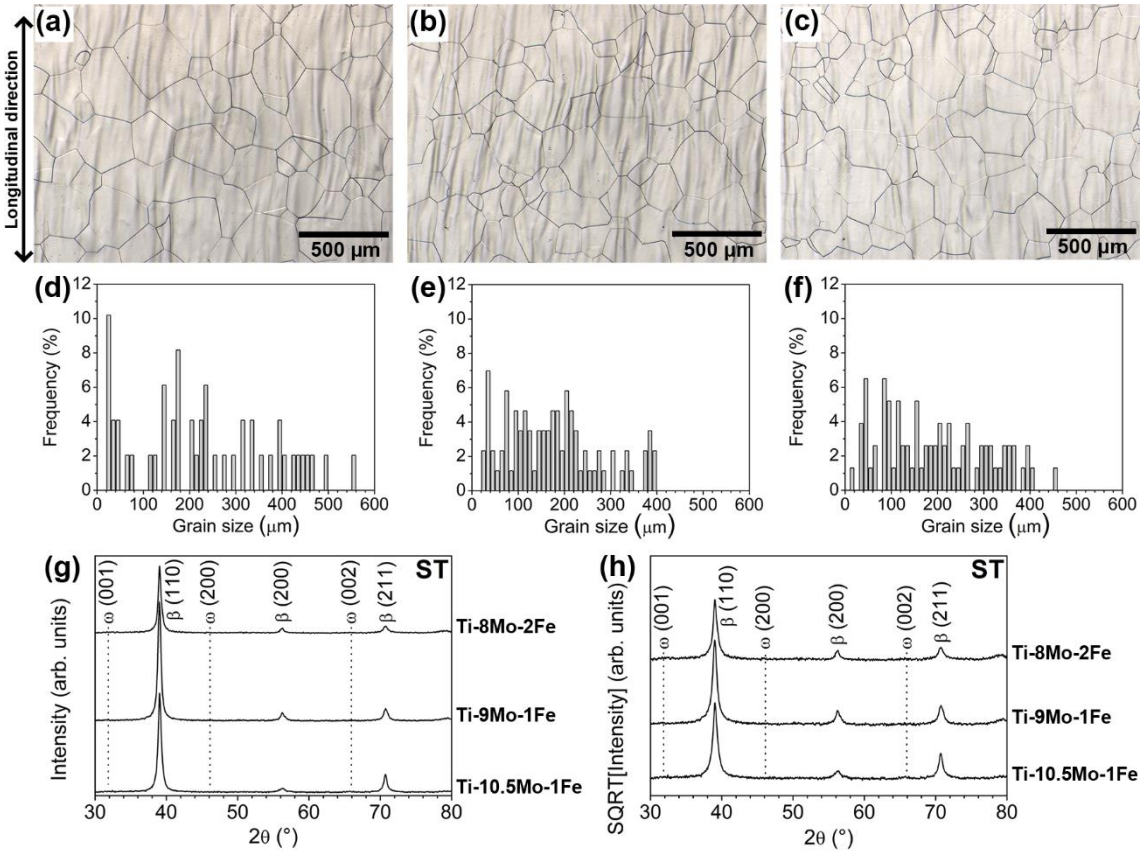

Fig. 2. Optical micrographs (25 x) of (a) Ti-8Mo-2Fe, (b) Ti-9Mo-1Fe and (c) Ti-10.5Mo-1Fe alloys in the solution-treated condition. The observed plane is the axial section of the

cylindrical specimen and the vertical direction is parallel to the longitudinal direction. Grain size distribution for (d) Ti-8Mo-2Fe, (e) Ti-9Mo-1Fe and (f) Ti-10.5Mo-1Fe alloys obtained from low magnification EBSD maps containing 49, 86 and 77 non-border grains. XRD patterns of the alloys after solution treatment (ST) plotted in linear (g) and in square root (SQRT) intensity scale (h).

In order to investigate the structure of the samples, TEM analyses were performed on all alloys in the solution-treated condition. The athermal ω phase was present in all the samples in the form of nanometric precipitates. In particular, the inset of Fig. 3 (a) shows a typical selected area electron diffraction (SAED) pattern of the Ti-8Mo-2Fe alloy taken in Ti_{β} [-110] zone axis orientation. The most intense diffraction spots were due to Ti β-phase, but other small diffraction spots, regularly distributed, were visible and could be attributed to two variants of the athermal ω phase [37]. The TEM dark field image of Fig. 3 (a) was obtained by selecting the ω diffraction spot indicated in the inset. In this way, the ω precipitates, responsible for that diffraction spot, appeared brighter in the image and their distribution and size could be investigated. Comparing Fig. 3 (a) with Fig. 3 (b) and (c), obtained in the same experimental conditions for the Ti-9Mo-1Fe and Ti-10.5Mo-1Fe alloys, respectively, it was evident that the ω phase was present in all the alloys with a very similar distribution and size. Further TEM diffraction analyses performed on the alloys have evidenced a difference among the samples. Indeed, the SAED patterns of Ti-8Mo-2Fe and Ti-10.5Mo-1Fe, taken in Ti_{β} [111] zone axis orientation, were identical, Fig. 3 (d), but the corresponding SAED pattern of the Ti-9Mo-1Fe showed the presence of feeble diffraction spots regularly distributed, Fig. 3 (e). The geometry (blue cell in Fig. 3 (e)) and the interplanar distances associated to these small diffraction spots revealed the presence of the orthorhombic α" phase in [10-1] zone axis orientation. It is important to stress that the orientation relationships between the α" phase and Ti β matrix were in perfect agreement with those reported in literature [3]. The TEM dark field image

obtained with the α" (002) reflection is shown in Fig. 3 (f). The presence of a large number of small precipitates uniformly distributed inside the matrix was clearly visible. Probably, due to the small size of α" particles, the presence of this phase could not be inferred from the XRD pattern of this alloy.

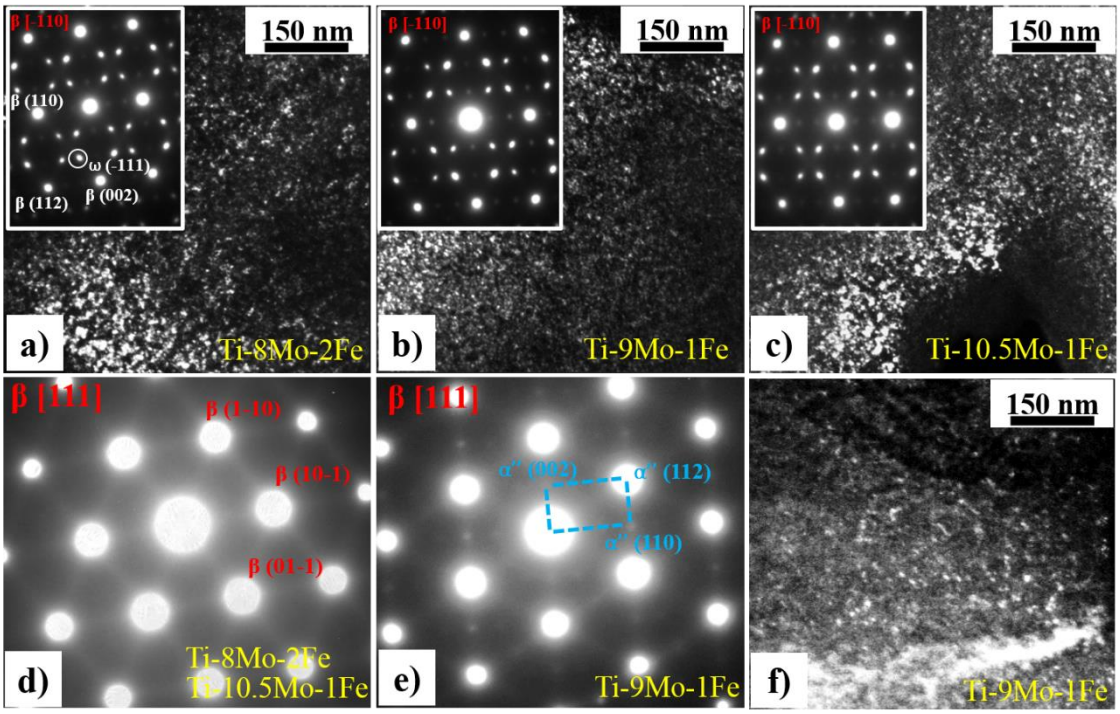

Fig. 3. Dark field TEM image and SAED pattern (inset) of (a) Ti-8Mo-2Fe, (b) Ti-9Mo-1Fe and (c) Ti-10.5Mo-1Fe alloys in the solution-treated condition showing the presence of the ω phase. SAED patterns taken in Ti_{β} [111] zone axis orientation of (d) Ti-8Mo-2Fe and Ti-10.5Mo-1Fe and (e) Ti-9Mo-1Fe showing the presence of the α" phase in this last alloy. (f) dark field TEM image showing the α" nanometric distribution in Ti-9Mo-1Fe.

The EPMA mappings of Mo and Fe in the solution-treated alloys are shown in Fig. 4: Fig. 4 (a-c) correspond to Mo distribution, while Fig. 4 (d-f) to Fe distribution. For each one of the three Ti-Mo-Fe alloys, the distribution of Mo and Fe was not homogeneous. An alternation of regions enriched and depleted with Mo and Fe was observed. In fact, the regions enriched and depleted with Mo were those corresponding respectively to low and high Fe content. This was attributed to the effect of solidification segregation, which was already reported in the literature for some β-stabilizer elements, including Mo, in Ti-

based alloys [38, 39]. The “stripes” observed in the optical micrographs of Fig. 2 were possibly caused by the difference of etching rates among regions that were rich and depleted in Mo (Fe), and consequently, more or less resistant to the etching process. Fig. 4 (g-i) show the elemental distribution of Ti, Mo and Fe along the white lines traced in the EPMA maps of Ti-8Mo-2Fe, Ti-9Mo-1Fe and Ti-10.5Mo-1Fe alloys, respectively. From Fig. 4 (g), it was observed that the minimum and maximum Mo content in Ti-8Mo-2Fe were 7.11 and 8.88 wt.%, while the minimum and maximum Fe content were 2.02 and 2.23 wt.%. In the Ti-9Mo-1Fe alloy (Fig. 4 (h)), 8.06 and 10.58 wt.% were the minimum and maximum Mo content, while Fe content varied between 1.08 and 1.21 wt.%. In the Ti-10.5Mo-1Fe alloy, Mo amount varied between 9.14 and 11.76 wt.%, while Fe amount was in the range 1.02 to 1.17 wt.%.

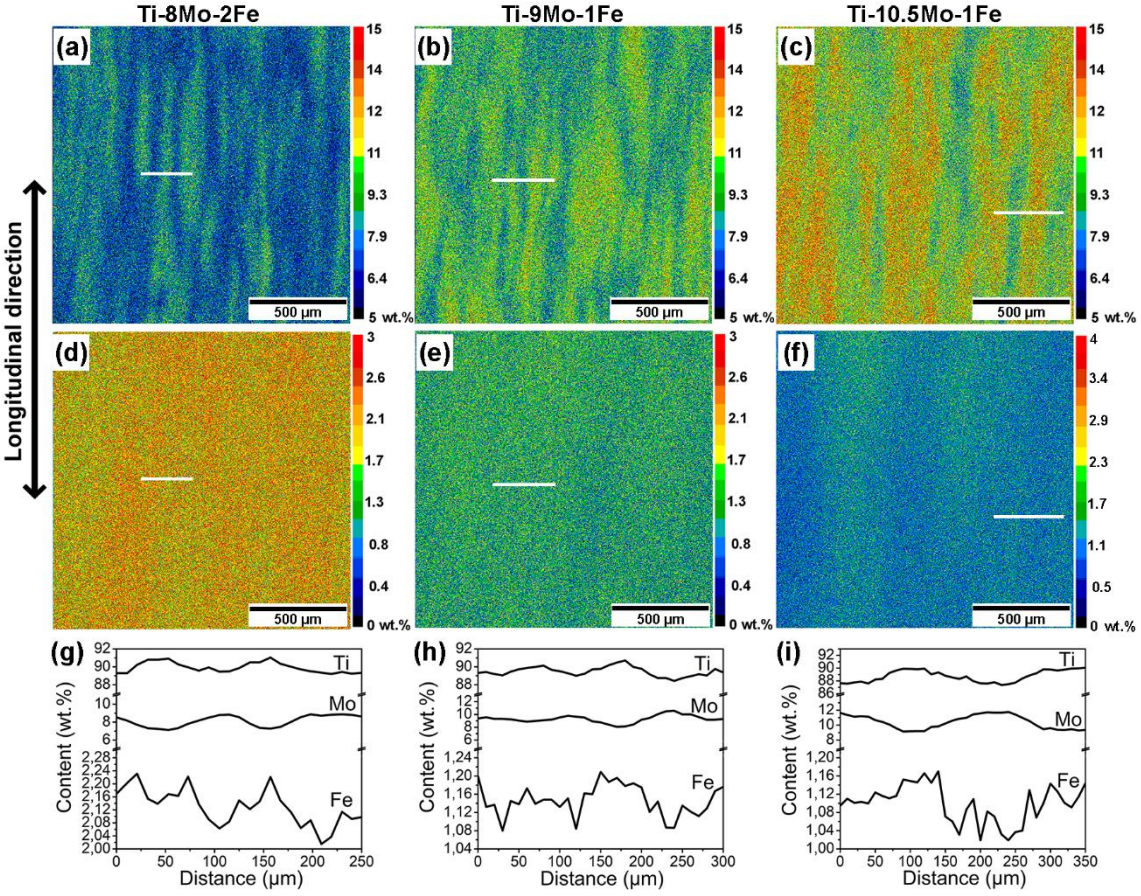

Fig. 4. EPMA mapping for Mo distribution in the solution-treated (a) Ti-8Mo-2Fe, (b) Ti-9Mo-1Fe and (c) Ti-10.5Mo-1Fe alloys. EPMA mapping for Fe distribution in the

solution-treated (d) Ti-8Mo-2Fe, (e) Ti-9Mo-1Fe and (f) Ti-10.5Mo-1Fe alloys. Elemental distribution of Ti, Mo and Fe along the white lines shown in the EPMA maps for (g) Ti-8Mo-2Fe, (h) Ti-9Mo-1Fe and (i) Ti-10.5Mo-1Fe.

3.2 Mechanical properties

Fig. 5 (a) shows the tensile nominal stress-strain curves of the Ti-Mo-Fe alloys. Their tensile mechanical properties and Vickers microhardness are listed in Table 2. Ti-9Mo-1Fe exhibited the highest microhardness (396 HV) among the studied alloys, while Ti-10.5Mo-1Fe exhibited the lowest microhardness of 346 HV. Ti-8Mo-2Fe presented an intermediary microhardness of 378 HV. Although a high ultimate tensile strength (UTS) of 1051 MPa and a high yield strength (YS) of 983 MPa were observed for Ti-9Mo-1Fe, it exhibited a poor ductility, with a total elongation (tEL) of 17% and a uniform elongation (uEL) of 6%. On the other hand, Ti-10.5Mo-1Fe was the alloy with the lowest UTS and YS, of 823 and 523 MPa, respectively. However, it exhibited the largest total and uniform elongations, of 46 and 34%, respectively. Ti-8Mo-2Fe combined high UTS (986 MPa) and YS (772 MPa) with large total (30%) and uniform (22%) elongations. Their elastic moduli (E) were between 97 (Ti-10.5Mo-1Fe) and 107 GPa (Ti-9Mo-1Fe); Ti-8Mo-2Fe presenting an intermediary value of 103 GPa.

The true stress-true strain curves and the corresponding work hardening rate as a function of the true strain are presented in Fig. 5 (b). High values of true stress were noted in the necking region: 1112 MPa for Ti-9Mo-1Fe, 1195 MPa for Ti-8Mo-2Fe and 1088 MPa for Ti-10.5Mo-1Fe. The true strain at necking, however, had a fairly different behavior. A very small true strain value of 6% occurred for Ti-9Mo-1Fe, while the highest value of 28% was presented by Ti-10.5Mo-1Fe. The intermediate true strain at necking of 19% was observed for Ti-8Mo-2Fe. Except for Ti-9Mo-1Fe, that showed limited work hardening capability, the other curves of work hardening rate gradually decreased in the

transition regime and became nearly stable in the plastic regime. The work hardening rate achieved 1120 MPa at a true strain of 28% for Ti-10.5Mo-1Fe, and 1370 MPa at a true strain of 19% for Ti-8Mo-2Fe.

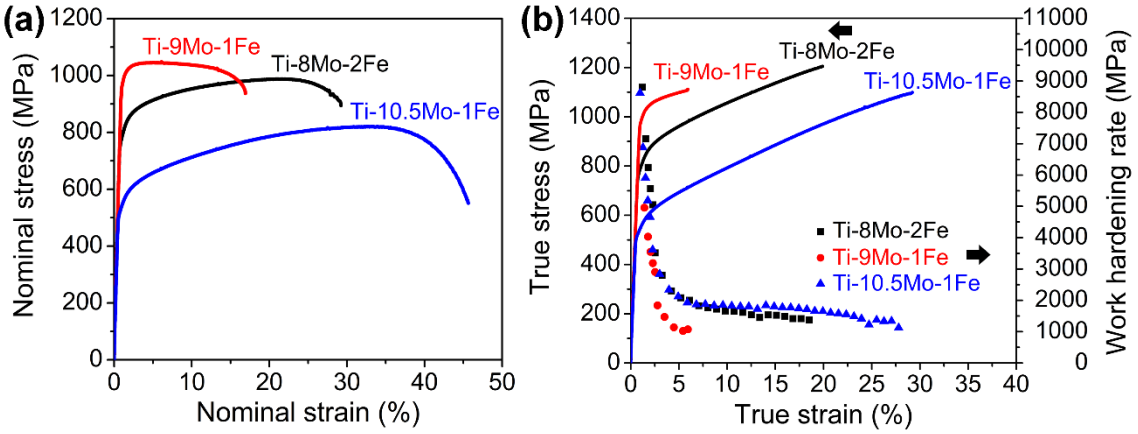

Fig. 5. (a) Tensile nominal stress-strain curves of Ti-Mo-Fe alloys tested at room temperature and strain rate of 10^{-3} s^{-1}; (b) true stress-true strain curves (solid lines) and the corresponding evolutions of work hardening rate with true strain (solid symbols).

Table 2. Vickers microhardness and tensile properties (YS - yield strength, UTS - ultimate tensile strength, uEL - uniform elongation, tEL - total elongation, E - elastic modulus measured by impulse excitation technique) of Ti-Mo-Fe alloys. Errors are reported in terms of standard deviation.

Alloy	Microhardness (HV)	YS (MPa)	UTS (MPa)	uEL (%)	tEL (%)	E (GPa)
Ti-8Mo-2Fe	378 ± 13	772 ± 3	986 ± 2	22 ± 0	30 ± 1	103 ± 0
Ti-9Mo-1Fe	396 ± 17	983 ± 9	1051 ± 5	6 ± 0	17 ± 2	107 ± 1
Ti-10.5Mo-1Fe	346 ± 8	523 ± 4	823 ± 3	34 ± 0	46 ± 2	97 ± 0

3.3 Microstructural characterization of the alloys after 3% total strain

Fig. 6 (a-c) are optical micrographs of, respectively, Ti-8Mo-2Fe, Ti-9Mo-1Fe and Ti-10.5Mo-1Fe alloys strained to 3% in tensile test. Plate-like features, which could be twins and/or stress-induced martensite (SIM), were observed in the three deformed alloys. Ti-9Mo-1Fe alloy exhibited a lower density of plate-like features when compared to Ti-8Mo-

2Fe and Ti-10.5Mo-1Fe alloys. Moreover, in the Ti-9Mo-1Fe alloy, line-like features, possibly dislocation lines [40], were also observed, as detailed in Fig. 6 (b). The nature of these deformation characteristics was described in the following EBSD and TEM sections, where a more detailed microstructural analysis was presented. Similarly to the solution-treated condition, the most intense peaks in the XRD patterns of the alloys strained to 3%, Fig. 6 (d) and (e), were due to β phase. The XRD patterns in square root intensity scale, Fig. 6 (e), also evidenced low intensity diffraction effects due to ω phase. The weight fraction of ω phase reduced after deforming the three alloys as can be seen in Table 3. The presence of SIM α" could not be inferred from XRD patterns of the strained alloys.

In a similar way to the ST condition, the lattice parameter of the β phase of strained Ti-9Mo-1Fe and Ti-10.5Mo-1Fe alloys was lower than the nominal value reported in the 89-4913 ICDD file. For the strained Ti-8Mo-2Fe alloy, the lattice parameter value of the β phase was identical to the nominal one. Regarding texture, Ti-8Mo-2Fe alloy also responded differently to deformation when compared to the other two alloys. In fact, while for Ti-9Mo-1Fe and Ti-10.5Mo-1Fe alloys an absence of texture was seen after deformation, the Ti-8Mo-2Fe alloy tended to develop a (211) texture (Fig. 6 (d)).

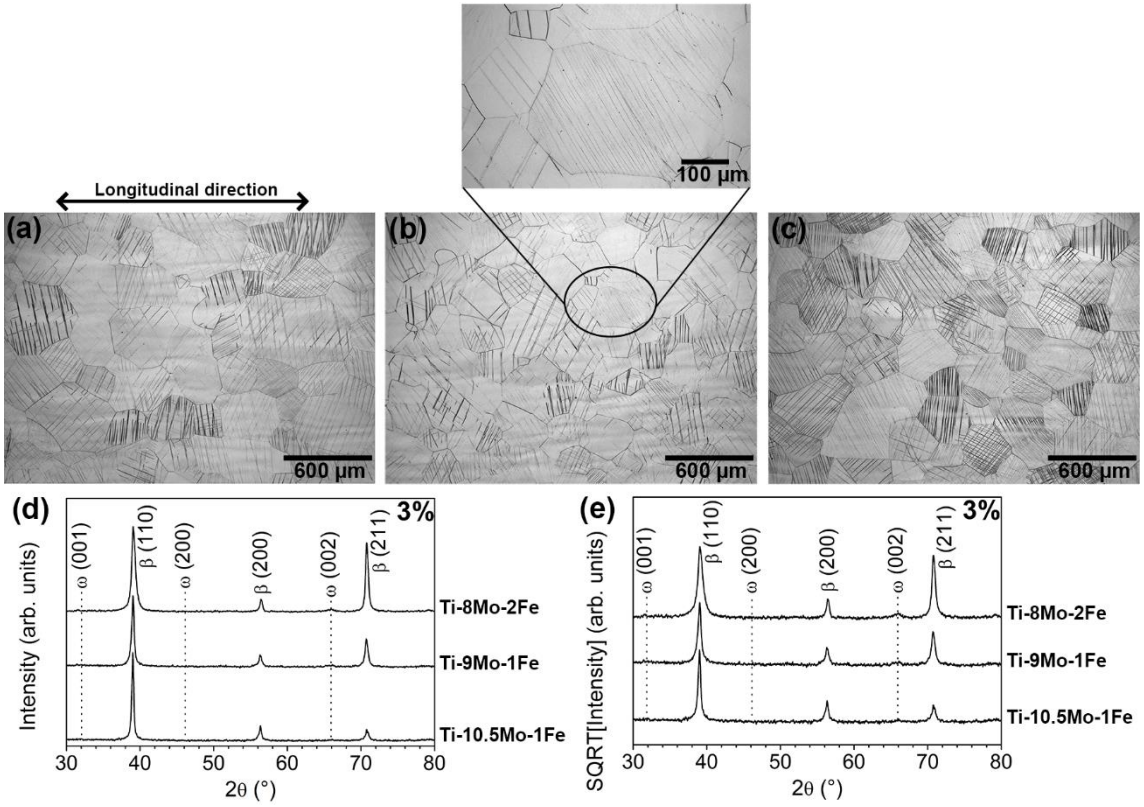

Fig. 6. Optical micrographs (50 x) of (a) Ti-8Mo-2Fe, (b) Ti-9Mo-1Fe and (c) Ti-10.5Mo-1Fe alloys strained to 3%. XRD patterns of the alloys after 3% strain (3%) plotted in linear (d) and in square root (SQRT) intensity scale (e).

Table 3. Lattice parameters of β and ω phases and weight fraction of the ω phase as estimated by the Rietveld analysis for alloys in ST and 3% conditions.

Sample	Condition	β-Ti Lattice par. (Å)	ω-Ti Lattice par. (Å)	Weight fraction (%)
Ti-8Mo-2Fe	ST	3.2660 ± 0.0009	4.612 ± 0.004 2.853 ± 0.003	35 ± 4
	3%	3.283 ± 0.003	4.620 ± 0.001 2.857 ± 0.003	31 ± 3
Ti-9Mo-1Fe	ST	3.2599 ± 0.0005	4.606 ± 0.004 2.842 ± 0.005	33 ± 2
	3%	3.2601 ± 0.0002	4.650 ± 0.006 2.836 ± 0.008	26 ± 5
Ti-10.5Mo-1Fe	ST	3.2643 ± 0.0005	4.612 ± 0.001 2.856 ± 0.003	45 ± 3
	3%	3.2524 ± 0.006	4.614 ± 0.003 2.830 ± 0.003	36 ± 2

EBSD analyses of the Ti-Mo-Fe alloys strained up to 3% are shown in Fig. 7 and Fig. 8. Fig. 7 shows EBSD band contrast maps (sections (a), (c) and (e), respectively of Ti-8Mo-2Fe, Ti-9Mo-1Fe and Ti-10.5Mo-1Fe), and the respective β phase inverse pole figure (IPF) maps (sections (b), (d) and (f)). Fig. 8 (a)-(c) exhibits the respective {332}<113> twins maps, where twin boundaries were delineated by the blue lines, and SIM α" phase was shown in red. Both {332}<113> twins and SIM α" phase were identified after straining the Ti-Mo-Fe alloys to 3%, as shown in Fig. 7 and Fig. 8. It was visibly seen from Fig. 8 (a) and (c) that in Ti-8Mo-2Fe and Ti-10.5Mo-1Fe, {332}<113> twinning was the predominant deformation mechanism. The quantification of {332}<113> twin density was shown in Fig. 8 (d). Ti-10.5Mo-1Fe was the alloy with highest twin density (0.13 μm^{-1}), followed by Ti-8Mo-2Fe with twin density of 0.09 μm^{-1} and by Ti-9Mo-1Fe alloy with twin density of 0.04 μm^{-1}. In all alloys, SIM α" occurred predominantly along the sides of the {332}<113> twins and no primary SIM α" band was detected by EBSD analyses. The presence of SIM α" at the twin/β matrix interface has been previously reported for other Ti alloys [41-43]. Fig. 8 suggested that the presence of SIM α" phase was more expressed in the deformed Ti-9Mo-1Fe alloy (Fig. 8 (b)). However, the SIM α" indexation in EBSD maps was affected by a relevant amount of noise; this was particularly evident for the condition Ti-9Mo-1Fe. For this reason, it was not possible a direct comparison of the SIM α" area fractions for all the studied conditions. A cause for the obstacles found in the analysis of the martensitic transformation was the fact that it occurred at a nanoscale level, approaching the spatial resolution limit of the used technique. The presence of nanometric SIM α", mainly at the twin/matrix interface, was therefore confirmed by TEM analyses (Fig. 10, Fig. S1 and Fig. S2 in supplementary data

document) and by transmission Kikuchi diffraction (TKD) analyses (Fig. S3 in the supplementary data document).

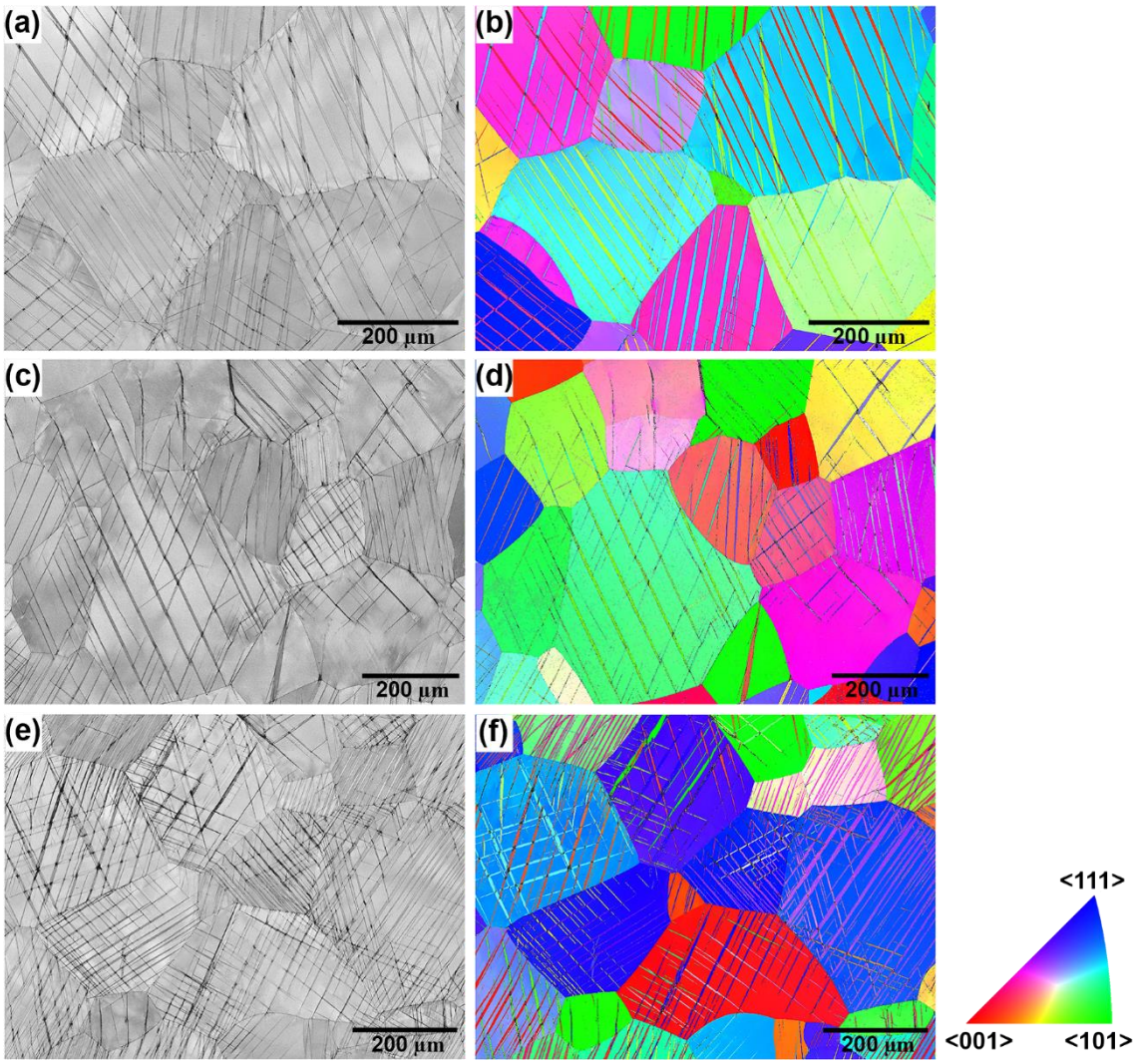

Fig 7. EBSD (a), (c) and (e) band contrast maps; and (b), (d) and (f) β phase sample normal direction inverse pole figure (IPF) maps of, respectively, Ti-8Mo-2Fe, Ti-9Mo-1Fe and Ti-10.5Mo-1Fe strained up to 3%.

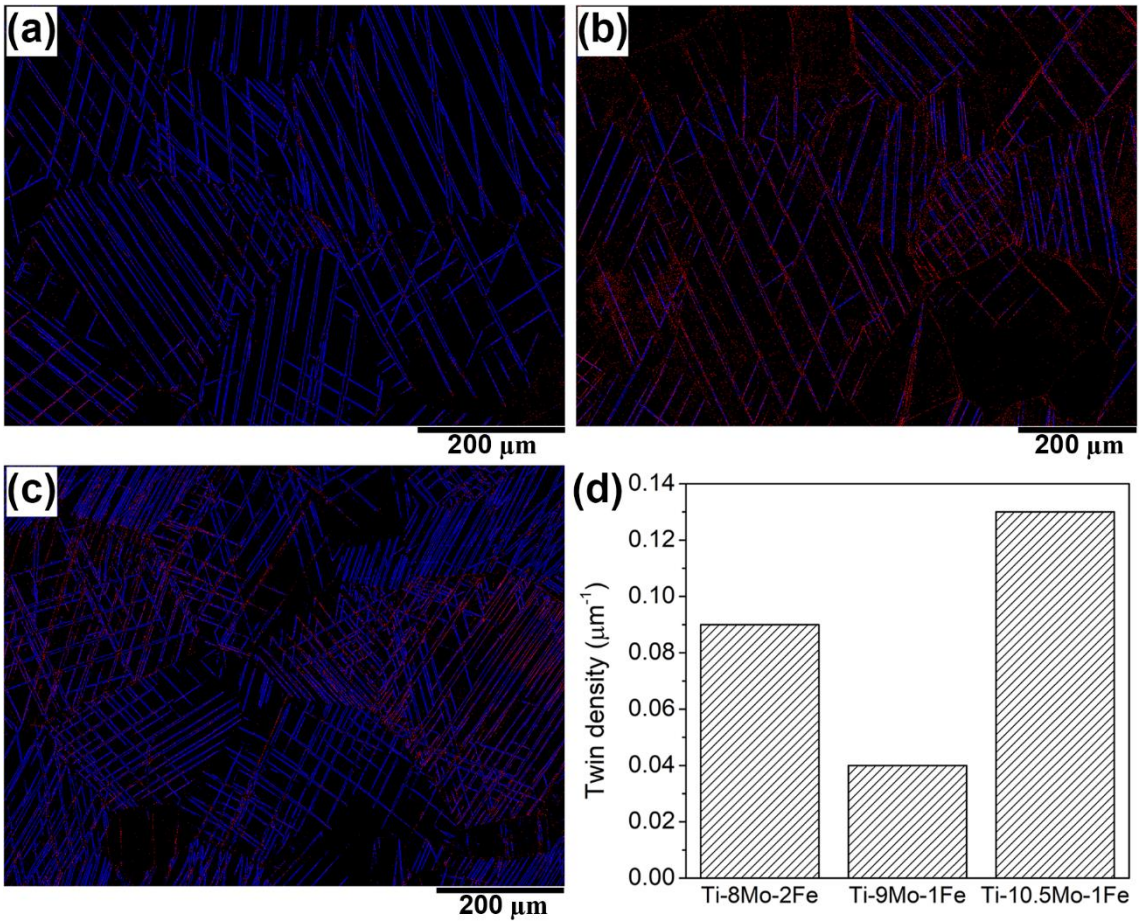

Fig. 8. EBSD {332}<113> twins (in blue) maps including stress-induced α" phase in red of (a) Ti-8Mo-2Fe, (b) Ti-9Mo-1Fe and (c) Ti-10.5Mo-1Fe strained up to 3%. SIM α" indexation was affected by a relevant amount of noise. (d) {332}<113> twin density in the Ti-Mo-Fe alloys strained up to 3%.

Transmission electron microscopy observations performed on the 3% strained samples confirmed the presence of {332}<113> twins in all the alloys. In detail, Fig. 9 (a) shows a TEM bright field image of a twin lamella inside the Ti-8Mo-2Fe alloy. The nature of the twin was revealed by the diffraction pattern taken in Ti_{β} [133] zone axis orientation, Fig. 9 (b), where the matrix (β) and the twin (βt) cells are evidenced in red and yellow, respectively. The dark field TEM image of Fig. 9 (c) was obtained with the twin diffraction spot encircled in the SAED pattern (Fig. 9 (b)) and, as expected, the lamella appeared brighter with respect to the matrix.

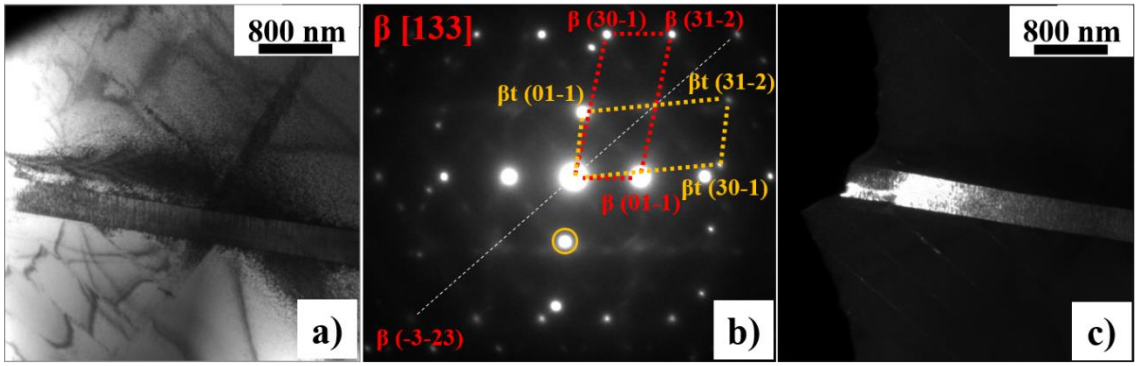

Fig. 9. Ti-8Mo-2Fe alloy 3% strained: (a) bright field TEM image of a {332}<113> twin; (b) corresponding SAED pattern showing the matrix (β) and the twin (βt) cells; (c) dark field TEM image obtained by using the encircled twin spot.

The SIM α" phase was identified by TEM in all the alloys, within twinned zones (secondary SIM α"). A typical bright field TEM image of SIM α" inside a {332}<113> twin is shown in Fig. 10 (a). The image refers to the Ti-8Mo-2Fe alloy; similar results were presented in the supplementary data document for Ti-9Mo-1Fe (Fig. S1) and Ti-10.5Mo-1Fe (Fig. S2). The α" phase was identified from the corresponding SAED pattern (Fig. 10 (b)) and the dark field image (Fig. 10 (c)) obtained by using the encircled α" reflection evidenced in the SAED pattern. The reflections coming from the twin (βt, red cell) and the SIM α" phase (blue cell) have been identified in the diffraction pattern. Fig. 10 (c) confirms what was previously observed from EBSD analyses (Fig. 8) and reported in the literature for Ti-7Mo-3Cr [41], that the SIM α" occurred predominantly at the twin interfaces.

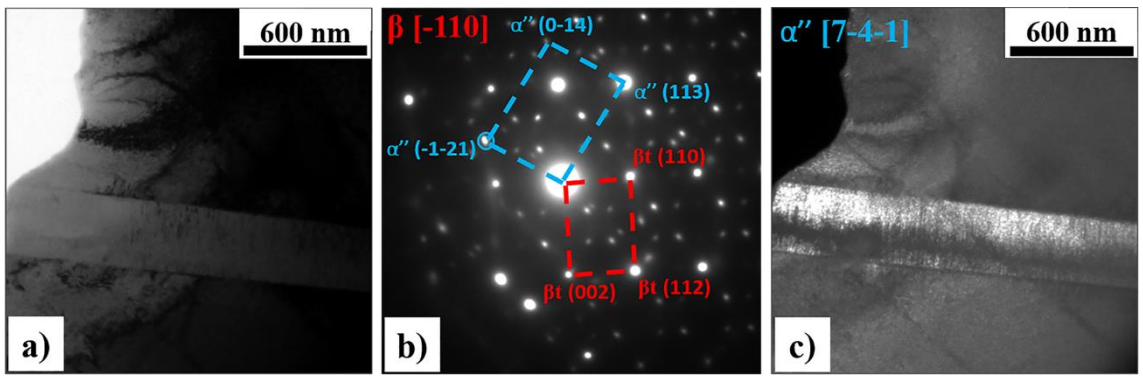

Fig. 10. Ti-8Mo-2Fe alloy 3% strained: (a) bright field TEM image of SIM α" inside a {332}<113> twin; (b) corresponding SAED pattern showing the twin (βt, red) and the SIM α" (blue) cells; (c) dark field TEM image obtained by using the encircled α" spot in the SAED.

Thin lamellar microstructures were observed by TEM for all the strained alloys. In detail, Fig. 11 (a) shows a bright field TEM image of a lamellar region in Ti-9Mo-1Fe alloy, while the corresponding SAED pattern was imaged in Fig. 11 (b). The diffraction pattern was taken in Ti_{β} [102] zone axis orientation and only diffraction spots coming from the Ti β phase and ω variants were present. Using the intense ω diffraction spot encircled in the SAED pattern, the dark field image of Fig. 11 (c) was obtained. This image clearly revealed that parallel thin lamellae were present, and they could be attributed to the presence of stress-induced ω phase. Concerning the strained Ti-9Mo-1Fe alloy, it is important to stress that SAED patterns taken in <111> zone axis orientation have never shown the presence of α" extra spot, on the contrary visible in the solution-treated condition. In particular, Fig. 11 (d) shows a typical Ti_{β} [111] electron diffraction pattern. Only diffraction spots coming from the Ti β matrix were visible revealing the strain-induced disappearance of the α" nanometric precipitates.

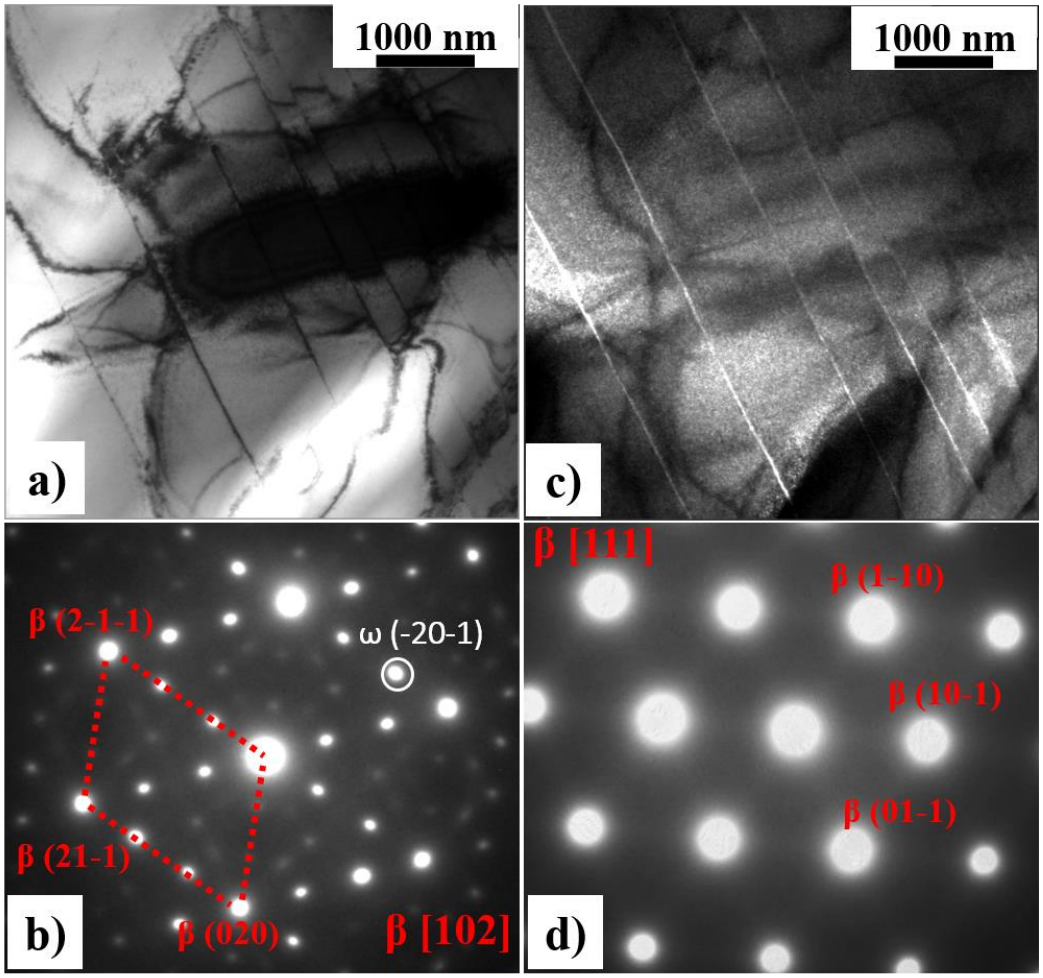

Fig. 11. Ti-9Mo-1Fe alloy 3% strained: (a) bright field TEM image showing thin lamellae; (b) corresponding SAED pattern; (c) dark field TEM image obtained by using the encircled ω spot in the SAED; (d) SAED pattern taken in Ti_{β} [111] zone axis.

4. Discussion

4.1. Phase stability of solution-treated and quenched alloys

In β metastable Ti alloys, with low content of β stabilizer elements such as Mo and Fe, β phase is not completely stable, as the name seems to suggest. The β phase can be retained by quenching these alloys from a temperature within the β field. However, depending on the stability of the β phase, other phases can precipitate during quenching, such as martensite and athermal ω phase. Martensite is formed in alloys with low β solute content, and its crystal structure changes from hexagonal close-packed (α') to orthorhombic (α") with the increase in β solute content. Athermal ω phase is formed in alloys with higher β

solute content compared to martensite, and its crystal structure changes from hexagonal to trigonal by increasing β solute content [3, 44, 45]. Due to the impact that these phases can have on the mechanical properties of Ti alloys, the prediction of their formation is of great interest. The Mo_{eq} parameter was designed to predict a Ti alloy tendency of retaining the β phase upon quenching [3, 46]. Although the calculation of this parameter was based on experimental data of binary alloys, it has been used as a guiding parameter for the design of multicomponent β Ti alloys [46]. It is generally accepted that alloys with Mo_{eq} higher than 10% retain β phase at room temperature, without martensite formation [46]. Table 4 shows the average, minimum and maximum Mo_{eq} values for the three studied alloys calculated from the variation of composition along the white lines draw in Fig. 4. The following formula [47, 48] was used for Mo_{eq} calculations:

$$[Mo]_{eq} = [Mo] + \frac{[Ta]}{5} + \frac{[Nb]}{3.6} + \frac{[W]}{2.5} + \frac{[V]}{1.5} + 1.25[Cr] + 1.25[Ni] + 1.7[Mn] + 1.7[Co] + 2.5[Fe] \quad (1)$$

where [x] corresponds to the concentration of the x-*th* element in weight percent [47].

Based on this, the presence of α" martensite precipitates in the β matrix of solution-treated and quenched Ti-9Mo-1Fe alloy, revealed by TEM analyses (Fig. 3 (e-f)), was not expected, even considering the segregation aspects (minimum Mo_{eq} calculated to be 11%). This parameter calculation was defined to predict correctly the microstructures of binary Ti alloys and not of ternary or other multicomponent alloys [46], which can explain its failure in predicting the absence of martensite in the solution-treated and quenched Ti-9Mo-1Fe alloy.

Bignon et al. [46] have recently defined a parameter named nucleation parameter, which allows to predict if martensite forms upon quenching. This definition was based on thermodynamics and micromechanics and on the assumption that the nucleation of martensite upon quenching requires an energy barrier to be surpassed. By calculating this

parameter for several alloys in the literature, binary and multicomponent alloys, and by considering their microstructures described in the literature, Bignon et al. [46] determined the value of the critical nucleation parameter. This critical nucleation parameter separates the martensitic alloys from the β alloys, which was graphically shown in Fig. 6 of [46]. Considering the position of two Ti-Mo-Fe alloys, Ti-10Mo-1Fe (alloy number 1) and Ti-15Mo-1Fe (alloy number 4), in Fig. 6 of [46], it can be seen that by decreasing Mo content (keeping iron as 1 wt.%), the nucleation parameter increases. Thus, Ti-9Mo-1Fe alloy should have higher nucleation parameter than Ti-10Mo-1Fe, which is slightly down the threshold horizontal line that is found to separate martensitic from β alloys. The Ti-9Mo-1Fe alloy is expected, thus, to be positioned above or along this threshold line, which suggests that martensite can be formed in this alloy upon quenching. Therefore, the presence of α" martensite in the solution-treated and quenched Ti-9Mo-1Fe alloy is consistent with the nucleation parameter model designed by Bignon et al. [46].

Interestingly, TEM analyses also revealed the coexistence of α" martensite and athermal ω precipitates in the solution-treated and quenched Ti-9Mo-1Fe alloy. It has been generally accepted that athermal ω phase formation during quenching occurs above M_s (martensite start) temperature, inhibiting the martensitic transformation [49]. However, according to Bignon et al. [46], the absence of martensite cannot be attributed to the presence of ω phase. In fact, they have computed using Thermo-Calc® the highest temperature at which ω transformation can occur upon quenching (T_0^{ω}), for a large number of alloys in the literature. They found that for several of them knowing to retain β phase, this temperature was lower than the calculated M_S^*, suggesting that ω phase forms below the temperature at which martensite should have formed [46]. Additionally, Cai et al. [50] and Li et al. [44] reported the coexistence of ω and martensite in quenched Ti-17Nb (at.%) and Ti-7.5Mo (wt.%) alloys, respectively, showing that the presence of ω

does not inhibit mandatorily martensite formation. Hildyard et al. [51] also observed the concurrent formation of α" and ω in a Ti-24Nb (at.%) alloy. Therefore, the coexistence of α" martensite and athermal ω precipitates in the β matrix of solution-treated and quenched Ti-9Mo-1Fe was thermodynamically possible.

4.2. Plastic deformation mechanisms

Stress-induced phase transformations

SIM α" was detected in all the 3% strained alloys by EBSD (Fig. 8) and TEM (Fig. 10, Fig. S1 and Fig. S2) analyses. These characterization techniques revealed that nanoscale stress-induced martensitic transformation occurred inside {332}<113> twins, mainly close to the twin/matrix interface. Such particularity has been previously reported for other Ti-based alloys, and two possible explanations have been explored. The first one hypothesizes that SIM α" is formed at the boundaries of deformation twins to accommodate stress concentration [42, 43, 52, 53]. In fact, high stresses are known to be generated in these areas [52], and SIM α" would precipitate as a relaxation mechanism. The second one hypothesizes that the stress-induced martensitic transformation mediates the formation of deformation twins [54, 55]. In order to completely understand the reason for SIM α" formation in the twin/matrix interfaces of the studied Ti-Mo-Fe alloys, an exhaustive study of the evolution of the deformation mechanisms in these alloys should be performed using in-situ techniques. Nonetheless, stress-induced martensitic transformation did not seem to act as a primary and major deformation mechanism in these alloys. At the studied strain level (3%), no primary band of SIM α" was detected in the β matrix of the alloys. Moreover, even for higher strain levels, the precipitation of SIM α" as a primary deformation mechanism is not expected since no “bump” was observed in their work hardening curves (Fig. 5 (b)). Indeed, a “bump” is generally observed in the work hardening rate curves of TWIP/TRIP Ti alloys and it is interpreted

as the contribution of β → SIM α" to the strain hardening of these alloys [41, 53]. Thus, it is reasonable to think that the SIM α" precipitation at the twin/matrix interfaces of the studied Ti-Mo-Fe alloys was acting as a local stress relaxation mechanism.

Therefore, the usage of the Bo-Md method (d-electron method) alone was not satisfactory to design the combination of TRIP and TWIP effects in Ti-Mo-Fe alloys. In other words, this method failed in predicting SIM α" as a primary deformation mechanism (primary TRIP effect) in both Ti-8Mo-2Fe and Ti-9Mo-1Fe alloys. The usage of this method in combination to the already mentioned nucleation parameter and to $[Fe]_{eq}$, an empirical parameter recently designed to predict the tendency to retain β upon deformation [46], would have led to better predictions. According to Bignon et al. [46], when the $[Fe]_{eq}$ value of a fully β Ti alloy (no martensite) is higher than 3.5 wt.%, it is expected that stress-induced martensitic transformation is inhibited (does not act as a primary deformation mechanism). The following equation was the one proposed by Bignon et al. [46] for $[Fe]_{eq}$ calculation:

$$[Fe]_{eq}=3.5x\left(\frac{[Fe]}{3.5}+\frac{[Cr]}{9}+\frac{[Mo]}{14}+\frac{[V]}{20}+\frac{[W]}{25}+\frac{[Sn]}{27}+\frac{[Nb]}{43}+\frac{[Ta]}{75}+\frac{[Zr]}{90}-\frac{[Al]}{18}\right)\ (wt.\%) \quad (2)$$

The success of the combination of these design approaches has been recently reported for a new β metastable Ti-7Cr-1Al-1Fe alloy [53]. For Ti-8Mo-2Fe alloy, although TRIP effect was expected by the Bo-Md method, its $[Fe]_{eq}$ value of 4 wt.% (nominal composition) would have suggested that TRIP was, in fact, not expected. Even when considering segregation aspects (minimum $[Fe]_{eq}$ of 3.9 wt.% as can be seen in Table 4), a TRIP effect was not foreseen for this alloy, which was confirmed by the experimental results. For Ti-9Mo-1Fe alloy, as already discussed, based on the critical nucleation parameter, quenching martensite was expected and confirmed by experimental results.

Thus, $[Fe]_{eq}$ parameter was not applicable and the Bo-Md method failed in predicting TRIP effect in this alloy. For Ti-10.5Mo-1Fe, both Bo-Md and $[Fe]_{eq}$ approaches (3.6 wt.% for nominal composition) suggested that stress-induced martensitic transformation was not expected as a primary deformation mechanism, which was confirmed by the experimental results. However, considering segregation aspects and $[Fe]_{eq}$ method (minimum $[Fe]_{eq}$ of 3.4 wt.%), in some regions the SIM transformation could have occurred as a primary deformation mechanism in Ti-10.5Mo-1Fe alloy.

It is worth noting that Min et al. [40] have studied the deformation mechanism of Ti-10Mo-1Fe alloy, with similar composition and segregation aspects as Ti-10.5Mo-1Fe alloy. Differently from the present study, no SIM α" was reported in Ti-10Mo-1Fe alloy after deformation. This difference could be related to the real absence of SIM α" in Ti-10Mo-1Fe due to its increased oxygen content (0.112 wt.%) when compared to the present study (0.05 wt.%) [37]. Another explanation is that SIM α" could in fact be present in Ti-10Mo-1Fe, but difficult to detect without the use of appropriate characterization techniques (for example, TEM analysis).

Table 4. Calculated average (avg.), minimum (min) and maximum (max) Mo equivalency (Mo_{eq}) and $[Fe]_{eq}$ based on the variation of Mo and Fe content (along white lines in Fig. 4) in the Ti-8Mo-2Fe, Ti-9Mo-1Fe and Ti-10.5Mo-1Fe alloys.

Alloy	Mo_{eq} (wt.%)			$[Fe]_{eq}$		
	Avg.	Min	Max	Avg.	Min	Max
Ti-8Mo-2Fe	13.5	12.5	14.2	4.2	3.9	4.3
Ti-9Mo-1Fe	12.2	11.0	13.3	-	-	-
Ti-10.5Mo-1Fe	13.2	12.0	14.4	3.7	3.4	4.0

In addition to SIM α", ω phase precipitation, in the form of parallel thin lamellae, occurred in all the 3% strained alloys (Fig. 11). Such a precipitation is known to occur by shear

stress and it was previously reported during the early stages of TWIP/TRIP Ti-12Mo plastic deformation [23]. It is worth noting that the studied Ti-Mo-Fe alloys exhibited athermal ω phase in their microstructures prior to deformation. Even with the precipitation of ω lamellae during deformation, the weight fraction of this phase was lower in the 3% strained alloys when compared to their solution-treated counterparts (Table 3). For Ti-12Mo alloy, Sun et al. [23] observed a slight increase of the ω phase fraction at the onset of plastic deformation, followed by a fast fraction reduction with increasing applied strain, until a complete disappearance of the same phase occurred. Shear band mechanism was proposed as explanation for this reduction and disappearance of ω phase. As suggested by Sun et al. [23] for Ti-12Mo alloy, ω particles in the studied Ti-Mo-Fe alloys could have been destroyed and reabsorbed by {112}<111> shear band formation, explaining the reduction of ω phase fraction after 3% strain.

Mechanical twinning

As expected by the design method, mechanical twinning was a primary deformation mechanism in the studied alloys. While SIM α" seemed to be acting as a stress relaxation mechanism in localized regions (mainly twin/matrix interfaces), mechanical twinning accommodated external loading. For Ti-8Mo-2Fe and Ti-10.5Mo-1Fe alloys, mechanical twinning was the major plastic deformation mechanism, and the formation of a dense network of {332}<113> twins could explain their high and steady work hardening rates. Indeed, mechanical twinning is known to be the main responsible for strain hardening in TWIP/TRIP Ti alloys due to the dynamic Hall-Petch effect (dynamic reduction of the mean free path of dislocations) [53, 56].

The twin density in Ti-9Mo-1Fe alloy was found to be lower compared to the other alloys (Fig. 8), and more precisely less than one third of Ti-10.5Mo-1Fe and less than a half of Ti-8Mo-2Fe. Several factors have been shown to affect mechanical twinning, that is grain

size, grain orientation, phase stability and interactions between twins and precipitates [27]. In terms of grain size, it is known that larger grains are more favorable to mechanical twinning than smaller ones [57]. All the studied alloys had large grains and a broad grain size distribution (Fig. 2). Therefore, grain size might not be the factor to explain the lower twin density in Ti-9Mo-1Fe. Regarding textural influence on mechanical twinning, Schmid factor analysis is often used; when Schmid factor is higher than 0.4, the grain is favorably oriented for twinning [57]. It is worth noting that from XRD analysis, an absence of texture was observed for all the ST Ti-Mo-Fe alloys. Schmid factor maps for the {332}<113> system are shown in Fig. S4 in the supplementary data document. It can be seen that all grains in the maps of Ti-8Mo-2Fe (Fig. S4 (a)) and Ti-10.5Mo-1Fe (Fig. S4 (b)) were favorably oriented for twinning. For Ti-9Mo-1Fe alloy (Fig. S4 (c)), there were some grains not favorably oriented for twinning (grain 1 for example). However, twinning is not only dependent on Schmid factor. In fact, in some grains favorably oriented for twinning (grain 2 and grain 3, for example), there was no nucleation of twins; while in some grains not favorably oriented (grain 1), twin nucleation occurred. Therefore, other factors seemed to have affected the mechanical twinning in Ti-9Mo-1Fe alloy. They could be mainly β phase stability [27] and the interactions of twins with quenched martensite precipitates.

It is known that deformation mechanism of β Ti alloys depends on their β phase stability (generally translated by Mo_{eq}). By increasing β phase stability, the deformation mechanism changes from stress-induced martensitic transformation to mechanical twinning and finally to dislocation slip [23, 37]. The absence of twins in some grains and even in some internal parts of some grains might be due to their lower β phase stability (Mo_{eq}) caused by the solidification segregation of β stabilizers [27, 38]. Indeed, Ti-9Mo-1Fe was the alloy with the lowest average and minimum Mo_{eq} values, on the basis of

element distribution after segregation, as can be seen from Table 4. Concerning interactions between precipitates and twins, athermal ω precipitates, which were present in all alloys, are known to be shear deformable and to have no impact on mechanical twinning [58, 59]. Although no prove was shown in the present work, no elemental partitioning should have been caused by martensitic precipitation during quenching, since this is a diffusionless thermally activated transformation [46]. Therefore, the stability of the β matrix should not have increased due to martensitic precipitation and cannot explain the reduced twin density in Ti-9Mo-1Fe alloy. Such reasoning can be valid when secondary precipitation of ω and α phases through aging treatments, involving diffusion of β stabilizing elements, occurs [59, 60]. However, other explanations have been given for the impact of precipitates on mechanical twinning, such as shear modulus difference between β matrix and precipitates. For Ti-25Nb-0.7Ta-2Zr, for example, the difference of shear modulus between β and nanometer-sized ω particles, precipitated during furnace cooling, was suggested as responsible for the suppression of {332}<113> deformation twinning [60].

Further analyses are required to understand how the quenched nanometer-sized martensitic particles could have affected the mechanical twinning in Ti-9Mo-1Fe alloy, and why these particles have disappeared after 3% straining as observed in Fig. 11 (d). However, it is reasonable to suppose that these nanometer-sized martensitic particles present only in ST Ti-9Mo-1Fe contributed to its lower twin density. The coexistence of these precipitates and athermal ω particles in the β matrix could possibly have hindered the mechanical twinning nucleation and/or multiplication.

To the best of our knowledge, the impact of quenched nanometer-sized α" particles (present only in the quenched Ti-9Mo-1Fe alloy (Fig. 3 (e-f)), on mechanical twinning has not been reported in the literature.

4.3. Mechanical properties

The work hardening rate curves of Ti-8Mo-2Fe and Ti-10.5Mo-1Fe alloys were different from the classic ones for TWIP/TRIP Ti alloys [53]. In fact, in the work-hardening curves of the studied alloys, no “bump” was observed since SIM α" did not act as a primary deformation mechanism in these alloys. They exhibited a typical work hardening rate curve of TWIP alloys [61]. Their work hardening rates were lower than the ones commonly observed for TWIP/TRIP Ti alloys [43, 56]. In fact, TWIP/TRIP Ti alloys exhibit higher work hardening rates due to the combined contribution of mechanical twinning and of primary stress-induced martensitic transformation [61]. In Ti-8Mo-2Fe and Ti-10.5Mo-1Fe alloys, the localized SIM α" (mainly at the twin/matrix interfaces) did not contribute to the strain hardening. However, their precipitation in these regions delayed the alloys fracture by accommodating stress concentration, contributing to the large ductility of these alloys [53]. The formation of a dense network of twins was the responsible for their relatively high and steady work hardening rates during all the plastic deformation regime [53], and consequently, for their large uniform elongations. Moreover, these alloys exhibited high UTS and YS; true stresses at necking and YS were comparable or even higher than the ones reported for TWIP/TRIP Ti alloys in literature [37, 43, 56]. The absence of stress-induced martensitic transformation (TRIP effect) as a primary deformation mechanism contributed to the higher YS of these alloys when compared to most TWIP/TRIP alloys [53]. Another contribution was the solid solution hardening by Fe, known as one of the most effective solid solution strengthening β stabilizer [28]. Regarding the higher YS and microhardness of Ti-8Mo-2Fe when compared to Ti-10.5Mo-1Fe alloy, one could expect the contrary, since the fraction of athermal ω phase (precipitation hardening) and the twin density were higher in the Ti-10.5Mo-1Fe alloy. However, in Ti-8Mo-2Fe alloy, the solid solution hardening by the Fe

might have been of greater contribution to the hardening than the athermal ω phase precipitation [40].

The mechanical properties of Ti-9Mo-1Fe alloy must be considered separately, mostly due to the presence of α" martensite prior to deformation (in the ST condition). It is suggested that the presence of these nanometer-sized α" particles together with athermal ω particles in the β matrix of Ti-9Mo-1Fe alloy could have hindered mechanical twinning, resulting in its limited work hardening capability and its small uniform elongation. Even if SIM α" acted as a stress-relaxation mechanism in Ti-9Mo-1Fe alloy, similarly than in the other studied alloys, its ductility was limited. Indeed, the presence of α" is known to decrease tensile ductility in Ti alloys [3]. It might also have contributed to the higher UTS, YS and microhardness observed for this alloy in comparison to Ti-8Mo-2Fe and Ti-10.5Mo-1Fe alloys [62].

5. Conclusions

Microstructural aspects, mechanical properties and plastic deformation mechanisms of three alloys of the Ti-Mo-Fe system, that is Ti-8Mo-2Fe, Ti-9Mo-1Fe and Ti-10.5Mo-1Fe, were investigated in the present work. The first two alloys were designed to combine TWIP/TRIP effects, while Ti-10.5Mo-1Fe alloy was designed to combine TWIP and dislocation slip as plastic deformation mechanisms. The design was guided by the Bo-Md method.

(1) Ti-9Mo-1Fe was the only alloy exhibiting nanometer-sized α" particles in the β matrix prior to deformation. Nanometer-sized athermal ω precipitates were also found in the β matrix of all studied alloys.

(2) The Bo-Md method alone failed in predicting TRIP effect in Ti-8Mo-2Fe and Ti-9Mo-1Fe alloys. However, in all the alloys, including Ti-10.5Mo-1Fe, stress-

induced martensite α" precipitated mainly in the {332}<113> twins/matrix interfaces, acting as a stress-relaxation mechanism.

(3) For Ti-8Mo-2Fe and Ti-10.5Mo-1Fe alloys, mechanical twinning was the main deformation mechanism. The formation of a dense network of {332}<113> twins was responsible for their high and steady work hardening rates over all the plastic regime. Work hardening rates of around 1370 and 1120 MPa were observed for Ti-8Mo-2Fe and Ti-10.5Mo-1Fe alloys, respectively. Consequently, these alloys exhibited large uniform elongations (22 and 34%, respectively). The SIM α" precipitation in twin/matrix interfaces also contributed to their large ductility, retarding the alloys fracture by accommodating localized stress concentration. Moreover, these alloys exhibited high yield strength (772 and 523 MPa, respectively) and ultimate tensile strength (986 and 823 MPa, respectively).

(4) Mechanical twinning was hindered in Ti-9Mo-1Fe (lowest twin density among the studied alloys), resulting in limited work hardening capability and small uniform elongation (6%). This alloy exhibited the highest yield strength (983 MPa) and ultimate tensile strength (1051 MPa). The hinder of mechanical twinning, the low ductility and high yield strength observed in this alloy are thought to be a consequence of the α" particles precipitated in the β matrix during quenching. However, further investigations are needed to understand how this nanometer-sized α" particles could have hindered mechanical twinning. It is also of interest to clarify if the coexistence of nanometer-sized α" and athermal ω particles in the β matrix of this alloy might have had a detrimental impact on mechanical twinning and on the ductility.

This work therefore showed that the design Bo-Md method alone was not always satisfactory to predict TRIP effects in β metastable Ti alloys. The joint use of this method

with other parameters, such as $[Fe]_{eq}$ and nucleation parameter proposed by Bignon et al. [46], is recommended for better predictions of TRIP effect and of martensitic precipitation during quenching. In any case, Ti-8Mo-2Fe and Ti-10.5Mo-1Fe alloys exhibited high strength-ductility trade-offs and relatively high work hardening rates when compared to TWIP/TRIP alloys. They might be competitive Ni-free alloys to replace 316L stainless steel and Co-Cr alloys for the manufacture of vascular stents.

Acknowledgements

C. C. Bortolan acknowledges the Fonds de Recherche du Québec Nature et Technologies (FRQNT) for the grant No. 279939. L. C. Campanelli is grateful to The Brazilian National Council for Scientific and Technological Development (CNPq) for the scholarship No. 150782/2019-5. This work was partially supported by the Natural Sciences and Engineering Research Council of Canada (Discovery, Strategic, Collaborative Research and Development, and College-University-Industry Programs), the Quebec Ministry of Economy and Innovation, the Canadian Foundation for Innovation, and the Regenerative Medicine Division of the University Quebec Hospital Research Center.

References

[1] L.C. Zhang, L.Y. Chen, A Review on Biomedical Titanium Alloys: Recent Progress and Prospect, Adv. Eng. Mater. 21 (2019) 1801215. https://doi.org/10.1002/adem.201801215.
[2] Q. Chen, G.A. Thouas, Metallic implant biomaterials, Mat. Sci. Eng. R 87 (2015) 1-57. https://doi.org/10.1016/j.mser.2014.10.001.
[3] I.J. Polmear, D. StJohn, J.-F. Nie, M. Qian, Light alloys : metallurgy of the light metals, fifth ed., Butterworth-Heinemann, Oxford, 2017.
[4] A.C.O. Tsang, P. Nicholson, V.M. Pereira, Nickel-Related Adverse Reactions in the Treatment of Cerebral Aneurysms: A Literature Review, World Neurosurg. 115 (2018) 147-153. https://doi.org/10.1016/j.wneu.2018.04.073.
[5] B. O'Brien, J. Stinson, W. Carroll, Initial exploration of Ti-Ta, Ti-Ta-Ir and Ti-Ir alloys: Candidate materials for coronary stents, Acta Biomater. 4 (2008) 1553-1559. https://doi.org/10.1016/j.actbio.2008.03.002.
[6] K. Cho, M. Niinomi, M. Nakai, J. Hieda, Y. Kawasaki, Development of High Modulus Ti-Fe-Cu Alloys for Biomedical Applications, Mater. Trans. 54 (2013) 574-581. https://doi.org/10.2320/matertrans.M2012361.
[7] Y. Tian, Z. Yu, C.Y. Ong, D. Kent, G. Wang, Microstructure, elastic deformation behavior and mechanical properties of biomedical beta-type titanium alloy thin-tube used for stents, J. Mech. Behav. Biomed. Mater. 45 (2015) 132-141. https://doi.org/10.1016/j.jmbbm.2015.02.001.
[8] J. Lin, S. Ozan, Y. Li, D. Ping, X. Tong, G. Li, C. Wen, Novel Ti-Ta-Hf-Zr alloys with promising mechanical properties for prospective stent applications, Sci. Rep. 6 (2016) 37901. https://doi.org/10.1038/srep37901.
[9] Y. Zhang, D. Kent, G. Wang, D. St John, M. Dargusch, An investigation of the mechanical behaviour of fine tubes fabricated from a Ti–25Nb–3Mo–3Zr–2Sn alloy, Mater. Des. 85 (2015) 256-265. https://doi.org/10.1016/j.matdes.2015.06.127.
[10] Y. Zhang, D. Kent, G. Wang, D. St John, M. Dargusch, Evolution of the microstructure and mechanical properties during fabrication of mini-tubes from a biomedical beta-titanium alloy, J. Mech. Behav. Biomed. Mater. 42 (2015) 207-218. https://doi.org/10.1016/j.jmbbm.2014.11.013.
[11] S. Yu, Z.-t. Yu, J.-y. Han, G. Wang, J.-l. Niu, M.S. Dargusch, Haemocompatibility of Ti–3Zr–2Sn–3Mo–25Nb biomedical alloy with surface heparinization using electrostatic self assembly technology, Trans. Nonferrous Met. Soc. China 22 (2012) 3046-3052. https://doi.org/10.1016/S1003-6326(11)61569-0.
[12] B. O'Brien, H. Zafar, A. Ibrahim, J. Zafar, F. Sharif, Coronary Stent Materials and Coatings: A Technology and Performance Update, Ann. Biomed. Eng. 44 (2016) 523-535. https://doi.org/10.1007/s10439-015-1380-x.
[13] J.A. Borovac, D. D'Amario, G. Niccoli, Neoatherosclerosis and Late Thrombosis After Percutaneous Coronary Intervention: Translational Cardiology and Comparative Medicine from Bench to Bedside, Yale J. Biol. Med. 90 (2017) 463–470.
[14] X. Liu, P. Chu, C. Ding, Surface modification of titanium, titanium alloys, and related materials for biomedical applications, Mater. Sci. Eng. R 47 (2004) 49-121. https://doi.org/10.1016/j.mser.2004.11.001.
[15] G. Mani, M.D. Feldman, D. Patel, C.M. Agrawal, Coronary stents: a materials perspective, Biomater. 28 (2007) 1689-1710. https://doi.org/10.1016/j.biomaterials.2006.11.042.

[16] P.P. Poncin, J. Proft, Stent Tubing: understanding the desired attributes. Materials & processes for medical devices conference, Anaheim, United States (8-10 September 2003) 253–259.
[17] A. Keshtta, M.A. Gepreel, Superelasticity Evaluation of the Biocompatible Ti-17Nb-6Ta Alloy, J. Healthc. Eng. 2019 (2019) 8353409. https://doi.org/10.1155/2019/8353409.
[18] Y.E. Saleh, M.A. Gepreel, N.K. Allam, Functional Nanoarchitectures For Enhanced Drug Eluting Stents, Sci. Rep. 7 (2017) 40291. https://doi.org/10.1038/srep40291.
[19] F. Prima, F. Sun, P. Vermaut, T.Gloriant, D. Mantovani, P.J. Jacques, High Performance Beta Titanium Alloys as a New Material Perspective for Cardiovascular Applications, Mater. Sci. Forum 706-709 (2012) 578-583. https://doi.org/10.4028/www.scientific.net/MSF.706-709.578.
[20] D.M. Gordin, F. Sun, D. Laillé, F. Prima, T. Gloriant, How a new strain transformable titanium-based biomedical alloy can be designed for balloon expendable stents, Materialia 10 (2020) 100638. https://doi.org/10.1016/j.mtla.2020.100638.
[21] M. Marteleur, F. Sun, T. Gloriant, P. Vermaut, P.J. Jacques, F. Prima, On the design of new β-metastable titanium alloys with improved work hardening rate thanks to simultaneous TRIP and TWIP effects, Scr. Mater. 66 (2012) 749-752. https://doi.org/10.1016/j.scriptamat.2012.01.049.
[22] P. Castany, T. Gloriant, F. Sun, F. Prima, Design of strain-transformable titanium alloys, C. R. Phys. 19 (2018) 710-720. https://doi.org/10.1016/j.crhy.2018.10.004.
[23] F. Sun, J.Y. Zhang, M. Marteleur, T. Gloriant, P. Vermaut, D. Laillé, P. Castany, C. Curfs, P.J. Jacques, F. Prima, Investigation of early stage deformation mechanisms in a metastable β titanium alloy showing combined twinning-induced plasticity and transformation-induced plasticity effects, Acta Mater. 61 (2013) 6406-6417. https://doi.org/10.1016/j.actamat.2013.07.019.
[24] F. Sun, F. Prima, T. Gloriant, High-strength nanostructured Ti–12Mo alloy from ductile metastable beta state precursor, Mater. Sci. Eng. A 527 (2010) 4262-4269. https://doi.org/10.1016/j.msea.2010.03.044.
[25] R.A. Byrne, M. Joner, A. Kastrati, Stent thrombosis and restenosis: what have we learned and where are we going? The Andreas Gruntzig Lecture ESC 2014, Eur. Heart J. 36 (2015) 3320-3331. https://doi.org/10.1093/eurheartj/ehv511.
[26] N. Foin, R.D. Lee, R. Torii, J.L. Guitierrez-Chico, A. Mattesini, S. Nijjer, S. Sen, R. Petraco, J.E. Davies, C. Di Mario, M. Joner, R. Virmani, P. Wong, Impact of stent strut design in metallic stents and biodegradable scaffolds, Int. J. Cardiol. 177 (2014) 800-808. https://doi.org/10.1016/j.ijcard.2014.09.143.
[27] X.H. Min, K. Tsuzaki, S. Emura, K. Tsuchiya, Enhancement of uniform elongation in high strength Ti–Mo based alloys by combination of deformation modes, Mater. Sci. Eng. A 528 (2011) 4569-4578. https://doi.org/10.1016/j.msea.2011.02.071.
[28] Y. Bao, M. Zhang, Y. Liu, J. Yao, Z. Xiu, M. Xie, X. Sun, High strength, low modulus and biocompatible porous Ti–Mo–Fe alloys, J. Porous Mater. 21 (2014) 913-919. https://doi.org/10.1007/s10934-014-9837-0.
[29] Q. Wang, C. Dong, P.K. Liaw, Structural Stabilities of β-Ti Alloys Studied Using a New Mo Equivalent Derived from [β/(α + β)] Phase-Boundary Slopes, Metall. Mater. Trans. A 46 (2015) 3440-3447. https://doi.org/10.1007/s11661-015-2923-3.
[30] X.H. Min, S. Emura, L. Zhang, K. Tsuzaki, Effect of Fe and Zr additions on ω phase formation in β-type Ti–Mo alloys, Mater. Sci. Eng. A 497 (2008) 74-78. https://doi.org/10.1016/j.msea.2008.06.018.
[31] M. Niinomi, M. Nakai, J. Hieda, Development of new metallic alloys for biomedical applications, Acta Biomater. 8 (2012) 3888-3903. https://doi.org/10.1016/j.actbio.2012.06.037.

[32] C. Brozek, F. Sun, P. Vermaut, Y. Millet, A. Lenain, D. Embury, P.J. Jacques, F. Prima, A β-titanium alloy with extra high strain-hardening rate: Design and mechanical properties, Scri. Mater. 114 (2016) 60-64. https://doi.org/10.1016/j.scriptamat.2015.11.020.
[33] M. Morinaga, Y. Murata, H. Yukawa, Molecular orbital approach to alloy design, in: G. Bozzolo, R.D. Noebe, P.B. Abdel, D. Vij (Eds.), Applied Computational Materials Modeling, Springer, Boston, 2007, pp. 255-306. https://doi.org/10.1007/978-0-387-34565-9_8.
[34] M. Abdel-Hady, K. Hinoshita, M. Morinaga, General approach to phase stability and elastic properties of β-type Ti-alloys using electronic parameters, Scr. Mater. 55 (2006) 477-480. https://doi.org/10.1016/j.scriptamat.2006.04.022.
[35] A.H.A. Pereira, L.B. Otani, R.J. A., N. Traon, T. Tonnessen, R. Telle, The influence of nonlinear elasticity on the accuracy of thermal shock damage evaluation by the impulse excitation technique, Interceram 60 (2011) 388-392.
[36] B. Beausir, J.-J. Fundenberger, Analysis Tools for Electron and X-Ray Diffraction, ATEX - Software, Université de Lorraine - Metz, (2017). www.atex-software.eu.
[37] C.C. Bortolan, L.C. Campanelli, C. Paternoster, N. Giguère, N. Brodusch, C. Bolfarini, R. Gauvin, P. Mengucci, G. Barucca, D. Mantovani, Effect of oxygen content on the mechanical properties and plastic deformation mechanisms in the TWIP/TRIP Ti–12Mo alloy, Mater. Sci. Eng. A 817 (2021) 141346. https://doi.org/10.1016/j.msea.2021.141346.
[38] X.H. Min, K. Tsuzaki, S. Emura, K. Tsuchiya, Heterogeneous twin formation and its effect on tensile properties in Ti–Mo based β titanium alloys, Mater. Sci. Eng. A 554 (2012) 53-60. https://doi.org/10.1016/j.msea.2012.06.009.
[39] J. Gao, J. Nutter, X. Liu, D. Guan, Y. Huang, D. Dye, W.M. Rainforth, Segregation mediated heterogeneous structure in a metastable beta titanium alloy with a superior combination of strength and ductility, Sci. Rep. 8 (2018) 7512. https://doi.org/10.1038/s41598-018-25899-3.
[40] X.H. Min, S. Emura, T. Nishimura, K. Tsuchiya, K. Tsuzaki, Microstructure, tensile deformation mode and crevice corrosion resistance in Ti–10Mo–xFe alloys, Mater. Sci. Eng. A 527 (2010) 5499-5506. https://doi.org/10.1016/j.msea.2010.06.016.
[41] J. Gao, Y. Huang, D. Guan, A.J. Knowles, L. Ma, D. Dye, W.M. Rainforth, Deformation mechanisms in a metastable beta titanium twinning induced plasticity alloy with high yield strength and high strain hardening rate, Acta Mater. 152 (2018) 301-314. https://doi.org/10.1016/j.actamat.2018.04.035.
[42] Y. Danard, R. Poulain, M. Garcia, R. Guillou, D. Thiaudière, S. Mantri, R. Banerjee, F. Sun, F. Prima, Microstructure design and in-situ investigation of TRIP/TWIP effects in a forged dual-phase Ti–10V–2Fe–3Al alloy, Materialia 8 (2019) 100507. https://doi.org/10.1016/j.mtla.2019.100507.
[43] L. Lilensten, Y. Danard, C. Brozek, S. Mantri, P. Castany, T. Gloriant, P. Vermaut, F. Sun, R. Banerjee, F. Prima, On the heterogeneous nature of deformation in a strain-transformable beta metastable Ti-V-Cr-Al alloy, Acta Mater. 162 (2019) 268-276. https://doi.org/10.1016/j.actamat.2018.10.003.
[44] M. Li, X. Min, K. Yao, F. Ye, Novel insight into the formation of α″-martensite and ω-phase with cluster structure in metastable Ti-Mo alloys, Acta Mater. 164 (2019) 322-333. https://doi.org/10.1016/j.actamat.2018.10.048.
[45] R. Kolli, A. Devaraj, A Review of Metastable Beta Titanium Alloys, Metals 8 (2018) 506. https://doi.org/10.3390/met8070506.

[46] M. Bignon, E. Bertrand, F. Tancret, P.E.J. Rivera-Díaz-del-Castillo, Modelling martensitic transformation in titanium alloys: The influence of temperature and deformation, Materialia 7 (2019), 100382. https://doi.org/10.1016/j.mtla.2019.100382.
[47] S. Ehtemam-Haghighi, Y. Liu, G. Cao, L.C. Zhang, Influence of Nb on the β → α″ martensitic phase transformation and properties of the newly designed Ti-Fe-Nb alloys, Mater. Sci. Eng. C 60 (2016) 503-510. https://doi.org/10.1016/j.msec.2015.11.072.
[48] R. Boyer, G. Welsch, E.W. Collings, Materials properties handbook : titanium alloys, ASM International, Metals Park, Ohio, 1994.
[49] Y. Al-Zain, H.Y. Kim, T. Koyano, H. Hosoda, T.H. Nam, S. Miyazaki, Anomalous temperature dependence of the superelastic behavior of Ti–Nb–Mo alloys, Acta Mater. 59 (2011) 1464-1473. https://doi.org/10.1016/j.actamat.2010.11.008.
[50] S. Cai, J.E. Schaffer, Y. Ren, Deformation of a Ti-Nb alloy containing α"-martensite and omega phases, Appl. Phys. Lett. 106 (2015) 131907. https://doi.org/10.1063/1.4916960.
[51] E.M. Hildyard, L.D. Connor, L.R. Owen, D. Rugg, N. Martin, H.J. Stone, N.G. Jones, The influence of microstructural condition on the phase transformations in Ti-24Nb (at.%), Acta Mater. 199 (2020) 129-140. https://doi.org/10.1016/j.actamat.2020.08.004.
[52] B. Qian, L. Lilensten, J. Zhang, M. Yang, F. Sun, P. Vermaut, F. Prima, On the transformation pathways in TRIP/TWIP Ti–12Mo alloy, Mater. Sci. Eng. A 822 (2021) 141672. https://doi.org/10.1016/j.msea.2021.141672.
[53] Y. Danard, G. Martin, L. Lilensten, F. Sun, A. Seret, R. Poulain, S. Mantri, R. Guillou, D. Thiaudière, I. Freiherr von Thüngen, D. Galy, M. Piellard, N. Bozzolo, R. Banerjee, F. Prima, Accommodation mechanisms in strain-transformable titanium alloys, Mater. Sci. Eng. A 819 (2021) 141437. https://doi.org/10.1016/j.msea.2021.141437.
[54] K. Cho, R. Morioka, S. Harjo, T. Kawasaki, H.Y. Yasuda, Study on formation mechanism of {332}<113> deformation twinning in metastable β-type Ti alloy focusing on stress-induced α" martensite phase, Scri. Mater. 177 (2020) 106-111. https://doi.org/10.1016/j.scriptamat.2019.10.011.
[55] M.J. Lai, C.C. Tasan, D. Raabe, On the mechanism of {332} twinning in metastable β titanium alloys, Acta Mater. 111 (2016) 173-186. https://doi.org/10.1016/j.actamat.2016.03.040.
[56] Y. Danard, F. Sun, T. Gloriant, I. Freiherr Von Thüngen, M. Piellard, F. Prima, The Influence of Twinning on the Strain–Hardenability in TRIP/TWIP Titanium Alloys: Role of Solute–Solution Strengthening, Front. Mater. 7 (2020). https://doi.org/10.3389/fmats.2020.00240.
[57] I. Gutierrez-Urrutia, C.L. Li, X. Ji, S. Emura, K. Tsuchiya, Quantitative analysis of {332}<113> twinning in a Ti-15Mo alloy by in situ scanning electron microscopy, Sci. Technol. Adv. Mater. 19 (2018) 474-483. https://doi.org/10.1080/14686996.2018.1475824.
[58] I. Gutierrez-Urrutia, C.L. Li, S. Emura, X. Min, K. Tsuchiya, Study of {332}<113> twinning in a multilayered Ti-10Mo-xFe (x = 1-3) alloy by ECCI and EBSD, Sci. Technol. Adv. Mater. 17 (2016) 220-228. https://doi.org/10.1080/14686996.2016.1177439.
[59] F. Sun, J.Y. Zhang, P. Vermaut, D. Choudhuri, T. Alam, S.A. Mantri, P. Svec, T. Gloriant, P.J. Jacques, R. Banerjee, F. Prima, Strengthening strategy for a ductile metastable β-titanium alloy using low-temperature aging, Mater. Res. Lett. 5 (2017) 547-553. https://doi.org/10.1080/21663831.2017.1350211.

[60] M.J. Lai, T. Li, D. Raabe, ω phase acts as a switch between dislocation channeling and joint twinning- and transformation-induced plasticity in a metastable β titanium alloy, Acta Mater. 151 (2018) 67-77. https://doi.org/10.1016/j.actamat.2018.03.053.
[61] G.-H. Zhao, X. Xu, D. Dye, P.E.J. Rivera-Díaz-del-Castillo, Microstructural evolution and strain-hardening in TWIP Ti alloys, Acta Mater. 183 (2020) 155-164. https://doi.org/10.1016/j.actamat.2019.11.009.
[62] S.E. Haghighi, H.B. Lu, G.Y. Jian, G.H. Cao, D. Habibi, L.C. Zhang, Effect of α″ martensite on the microstructure and mechanical properties of beta-type Ti–Fe–Ta alloys, Mater. Des. 76 (2015) 47-54. https://doi.org/10.1016/j.matdes.2015.03.028.

- Coexistence of α" and athermal ω particles was found in the β matrix of Ti-9Mo-1Fe.
- Nanometer α" particles in Ti-9Mo-1Fe are thought to hinder mechanical twinning.
- Bo-Md method failed in predicting TRIP effect in Ti-8Mo-2Fe and Ti-9Mo-1Fe alloys.
- Stress-induced martensite was mainly formed at twin/matrix interfaces.
- Stress-induced martensite acted as a stress-relaxation mechanism.

Figure 1

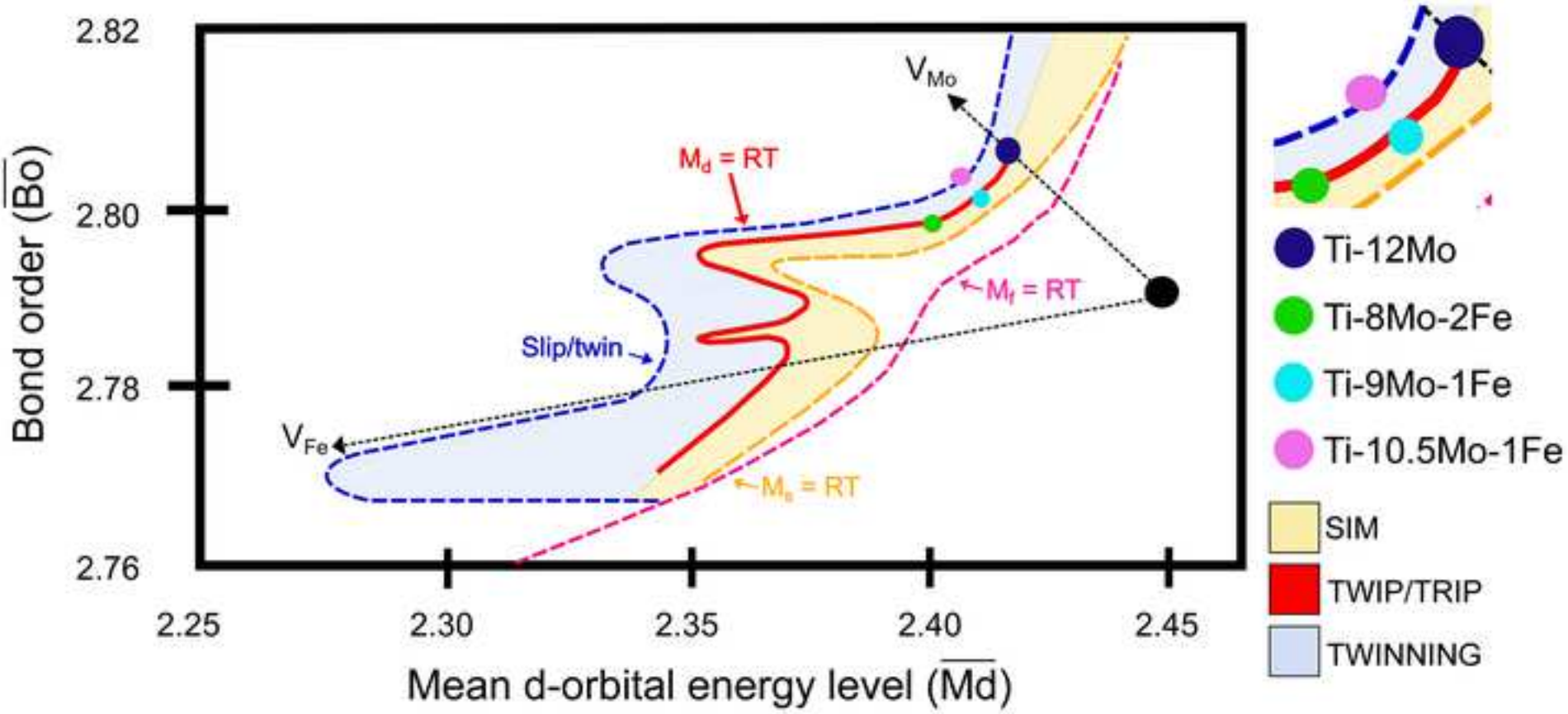

Figure 2

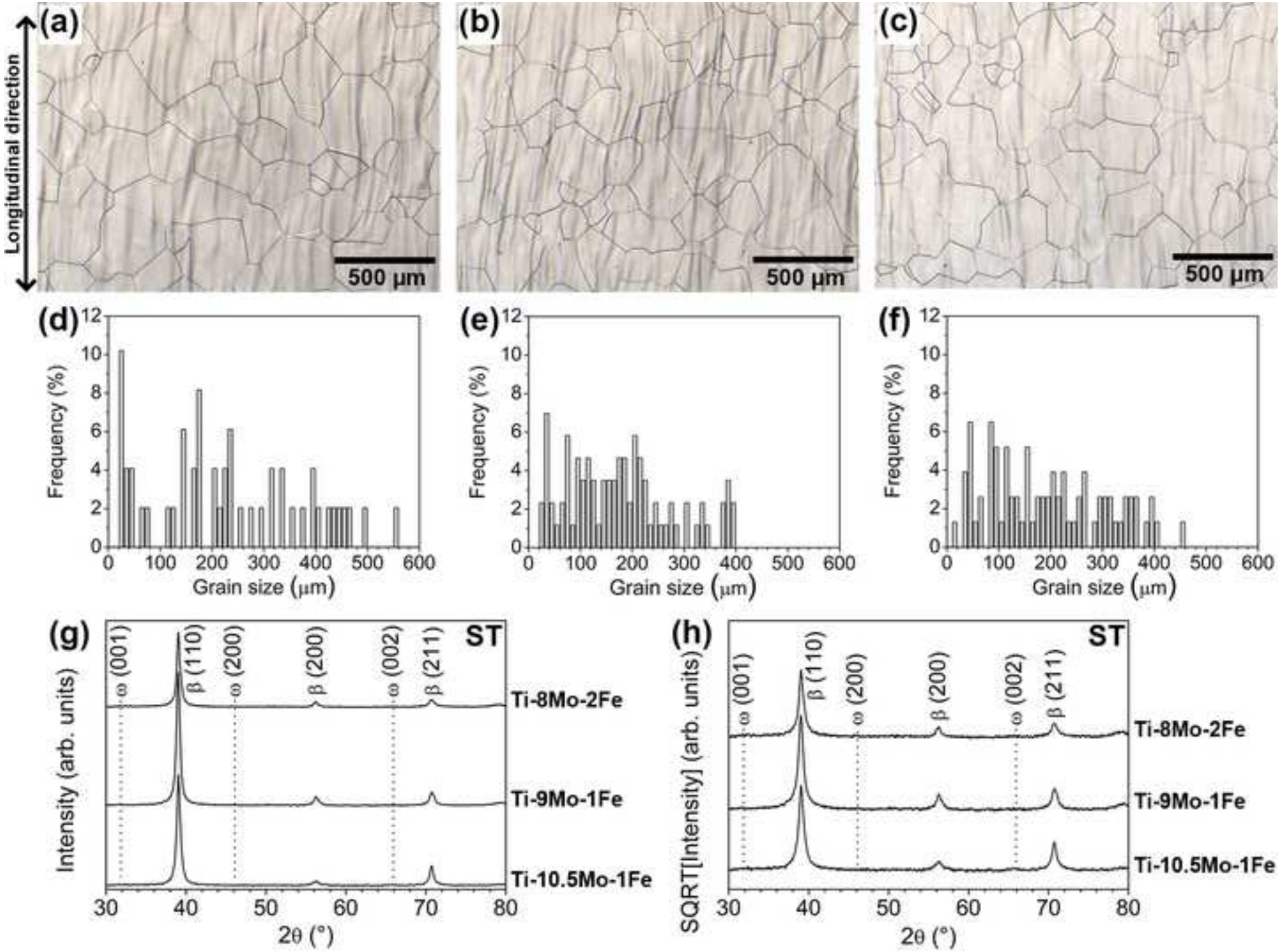

Figure 3

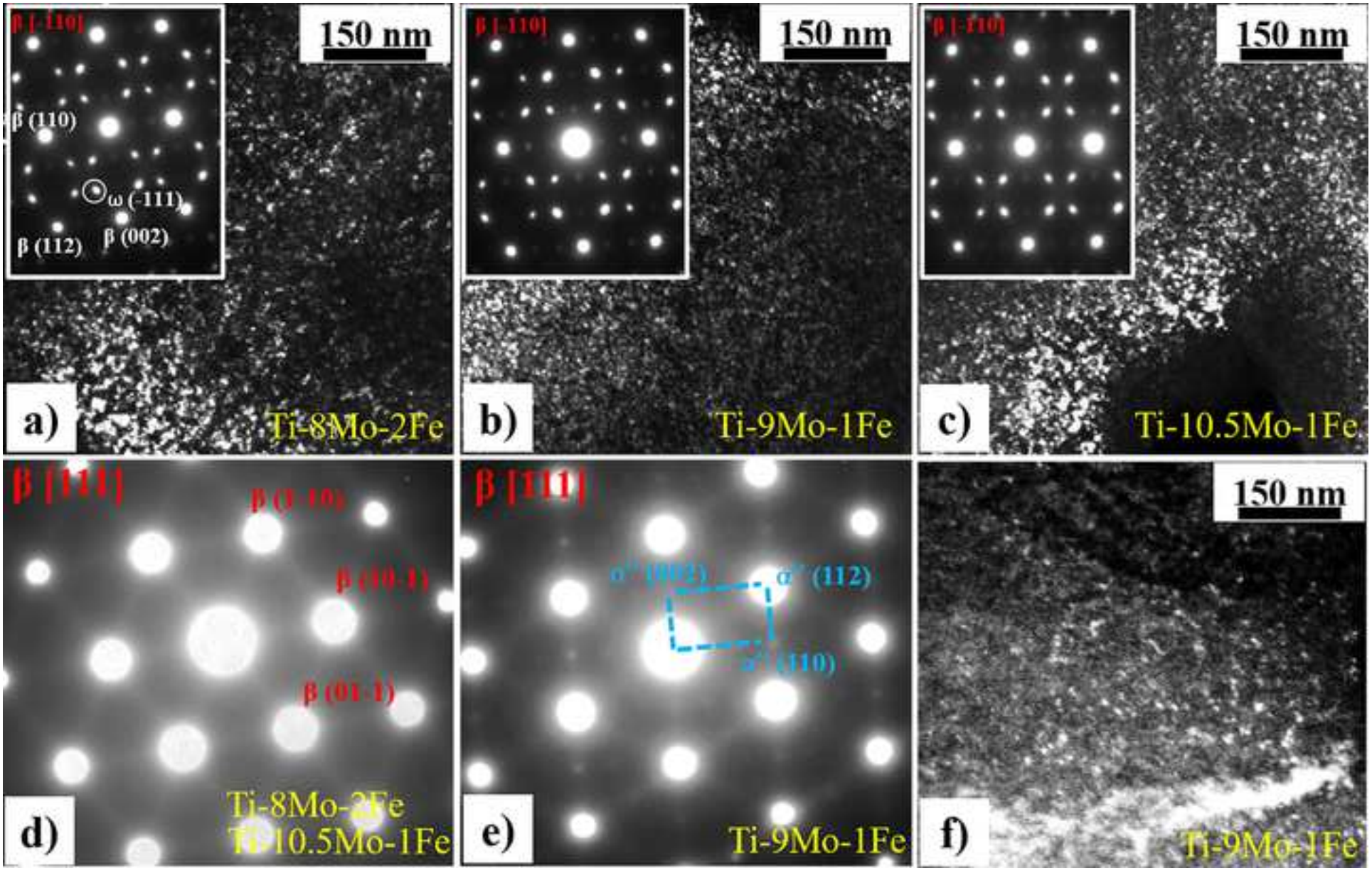

Figure 4

Click here to access/download;Figure;Fig. 4.tif

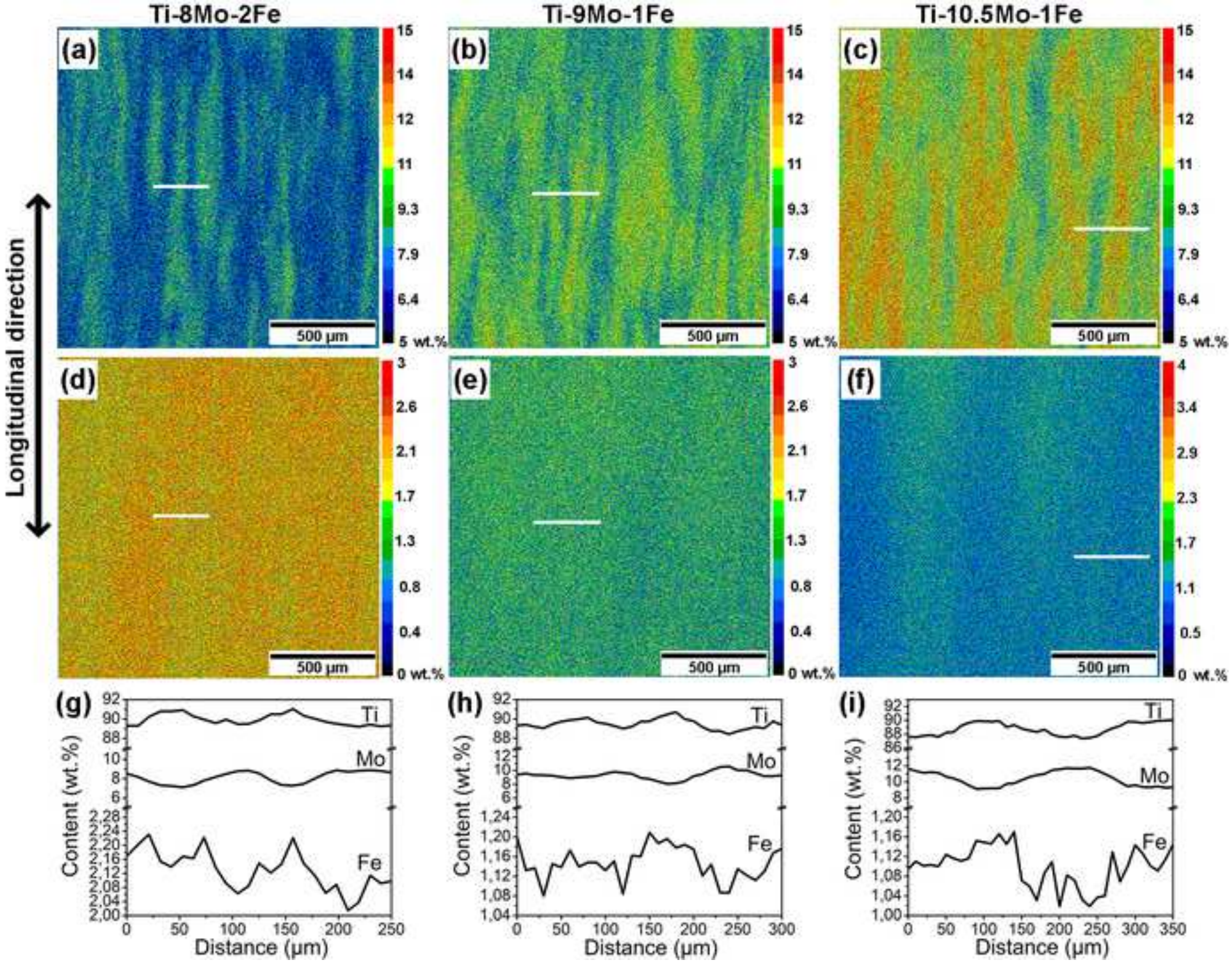

Figure 5

Click here to access/download;Figure;Fig. 5.tif

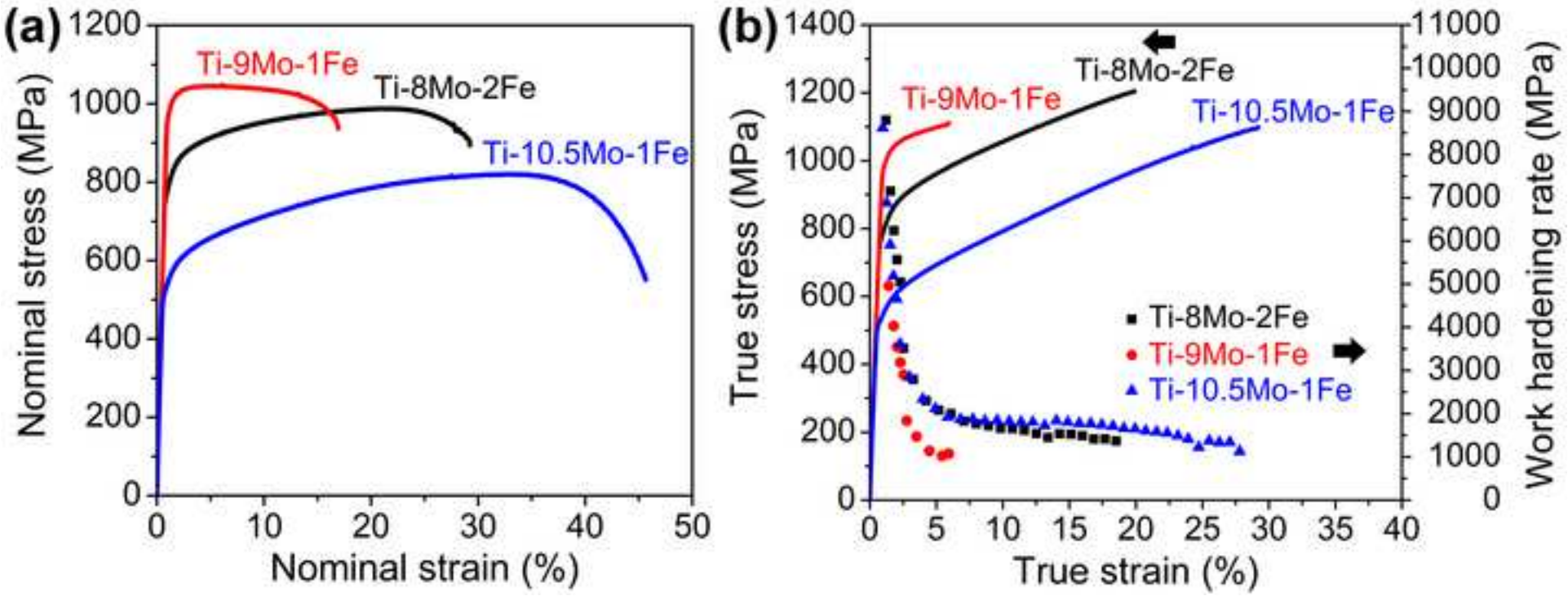

Figure 6

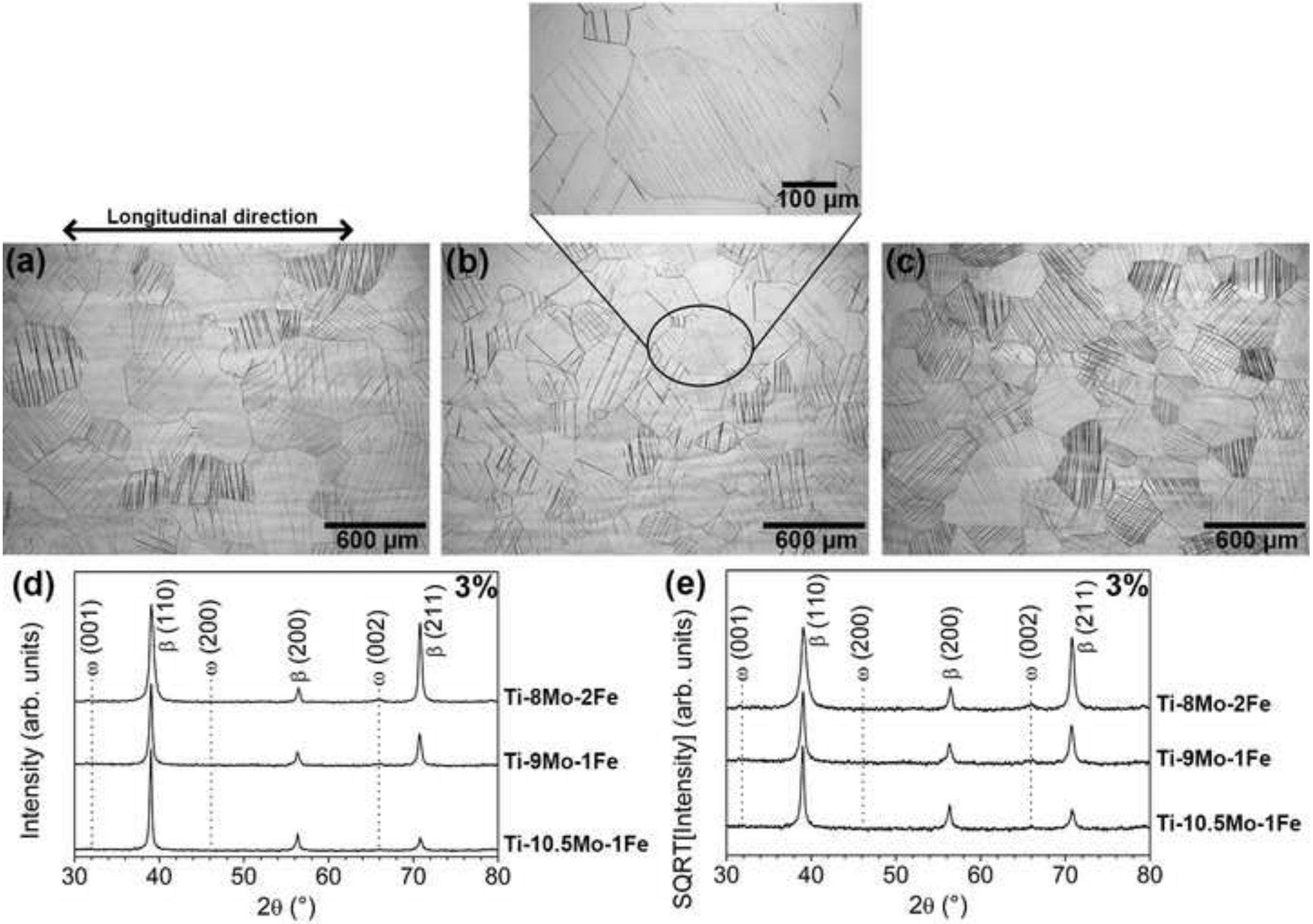

Figure 7

Click here to access/download;Figure;Fig. 7.tif

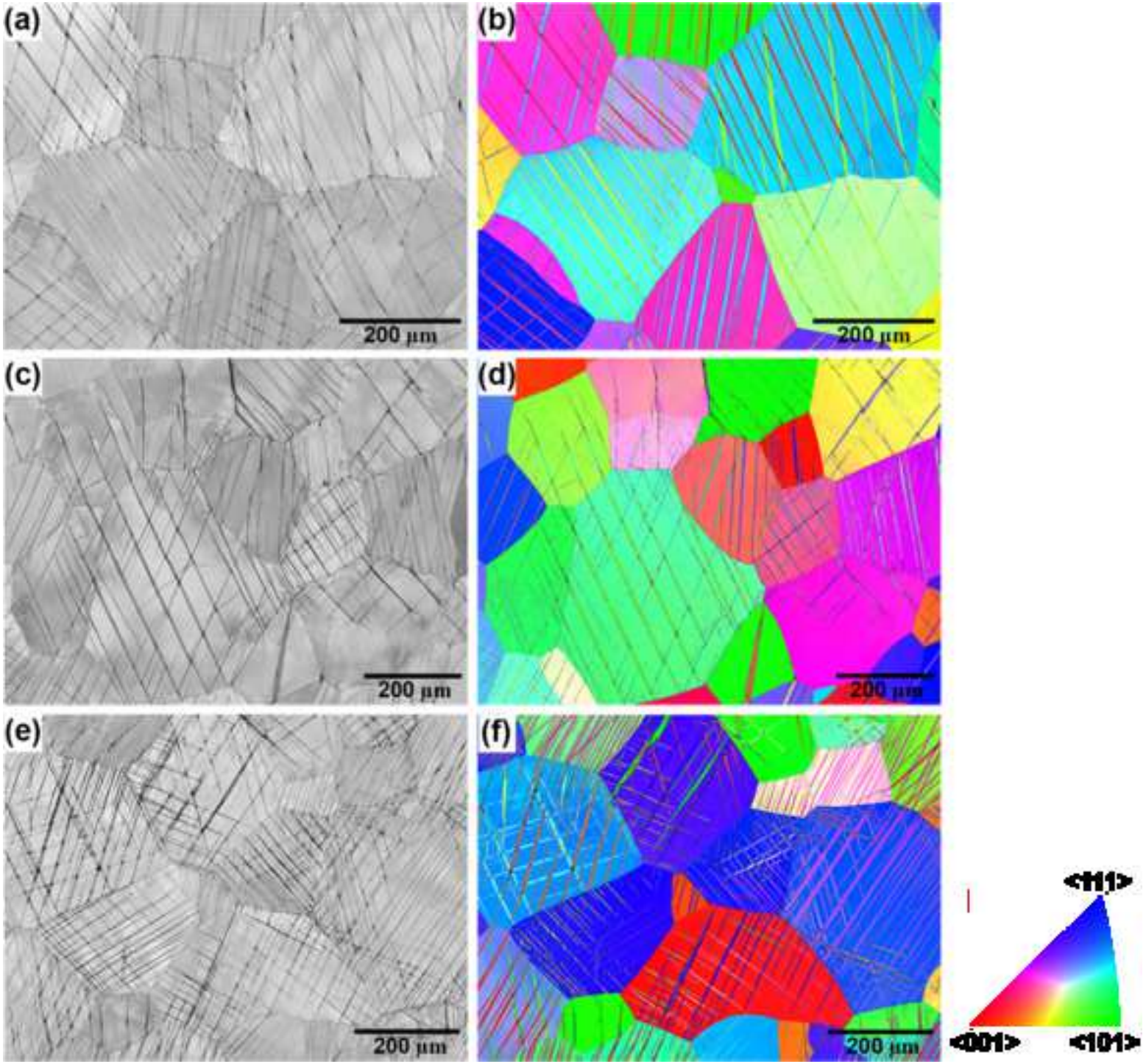

Figure 8

Click here to access/download;Figure;Fig. 8.tif

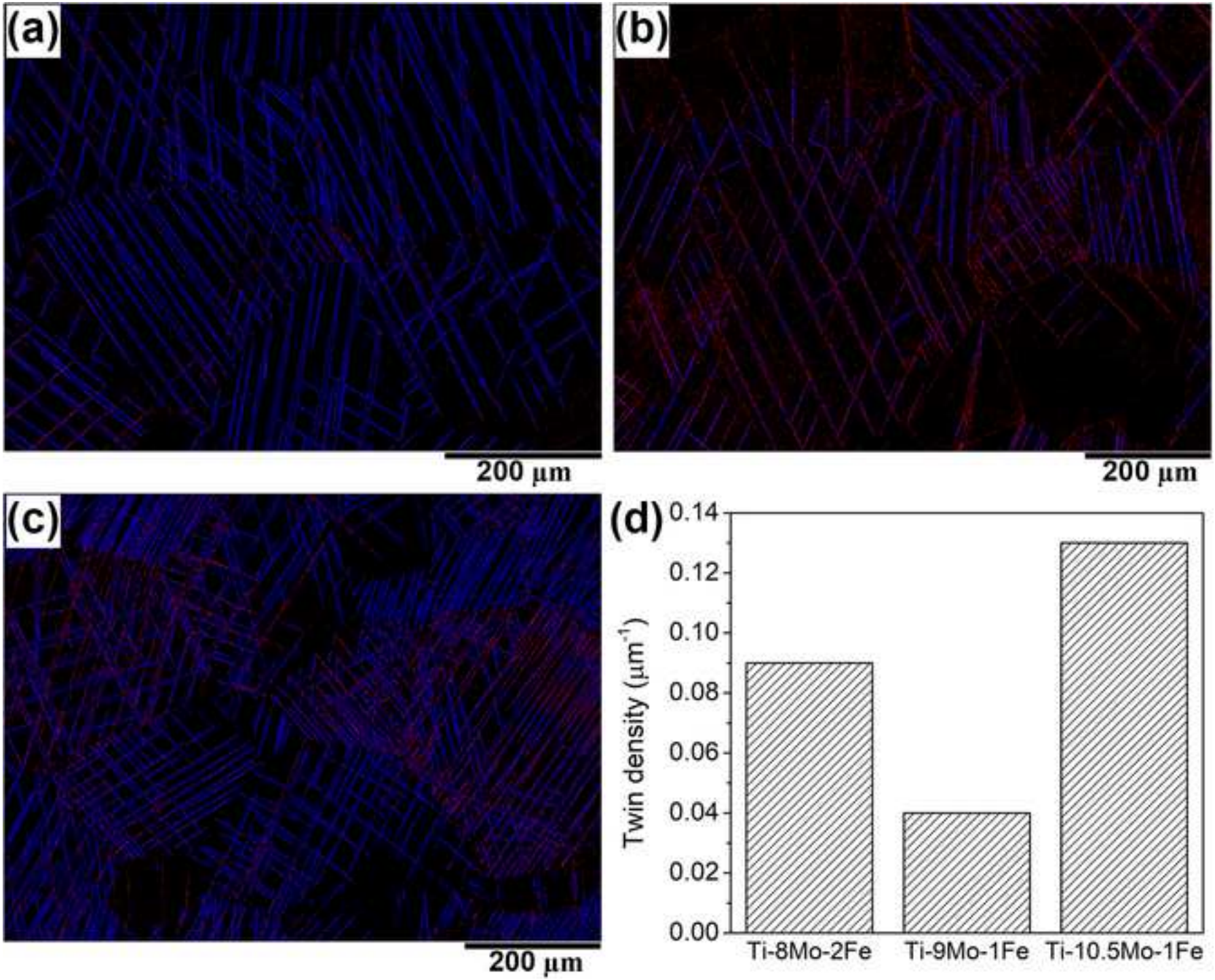

Figure 9

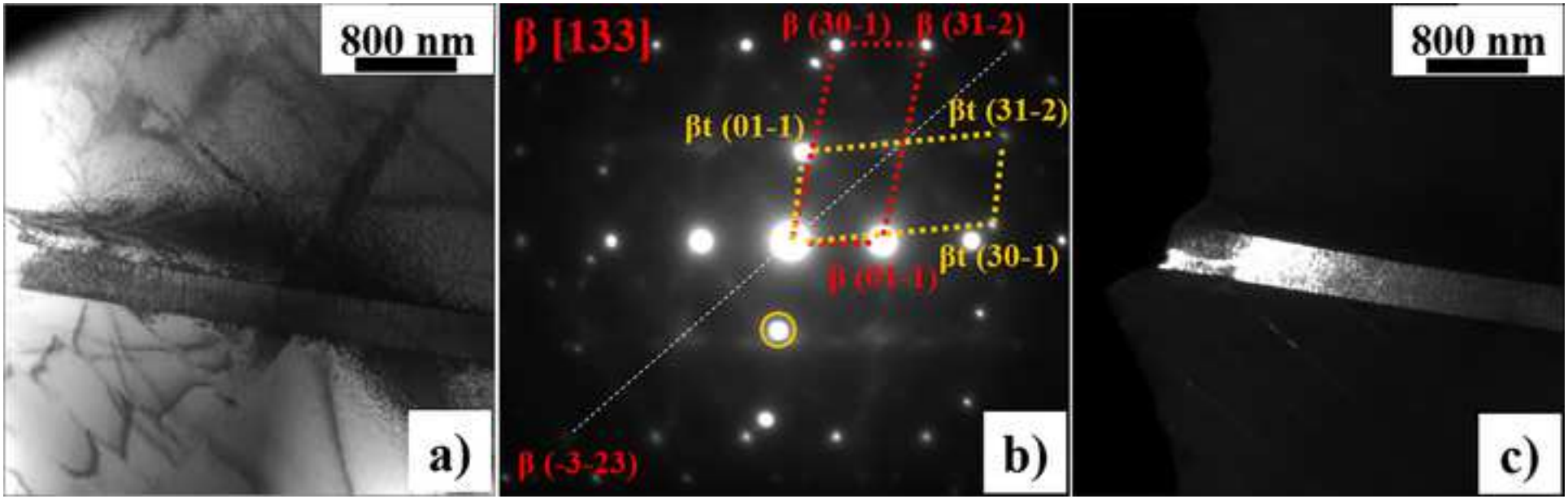

Figure 10

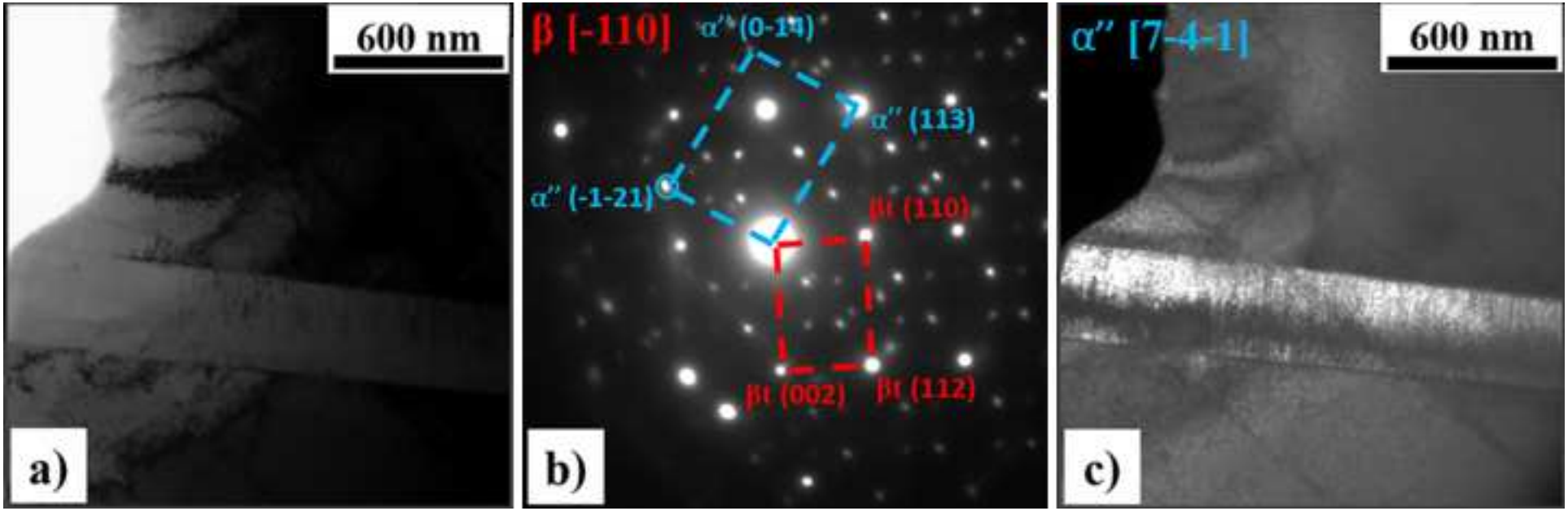

Figure 11

Click here to access/download;Figure;Fig. 11.tif

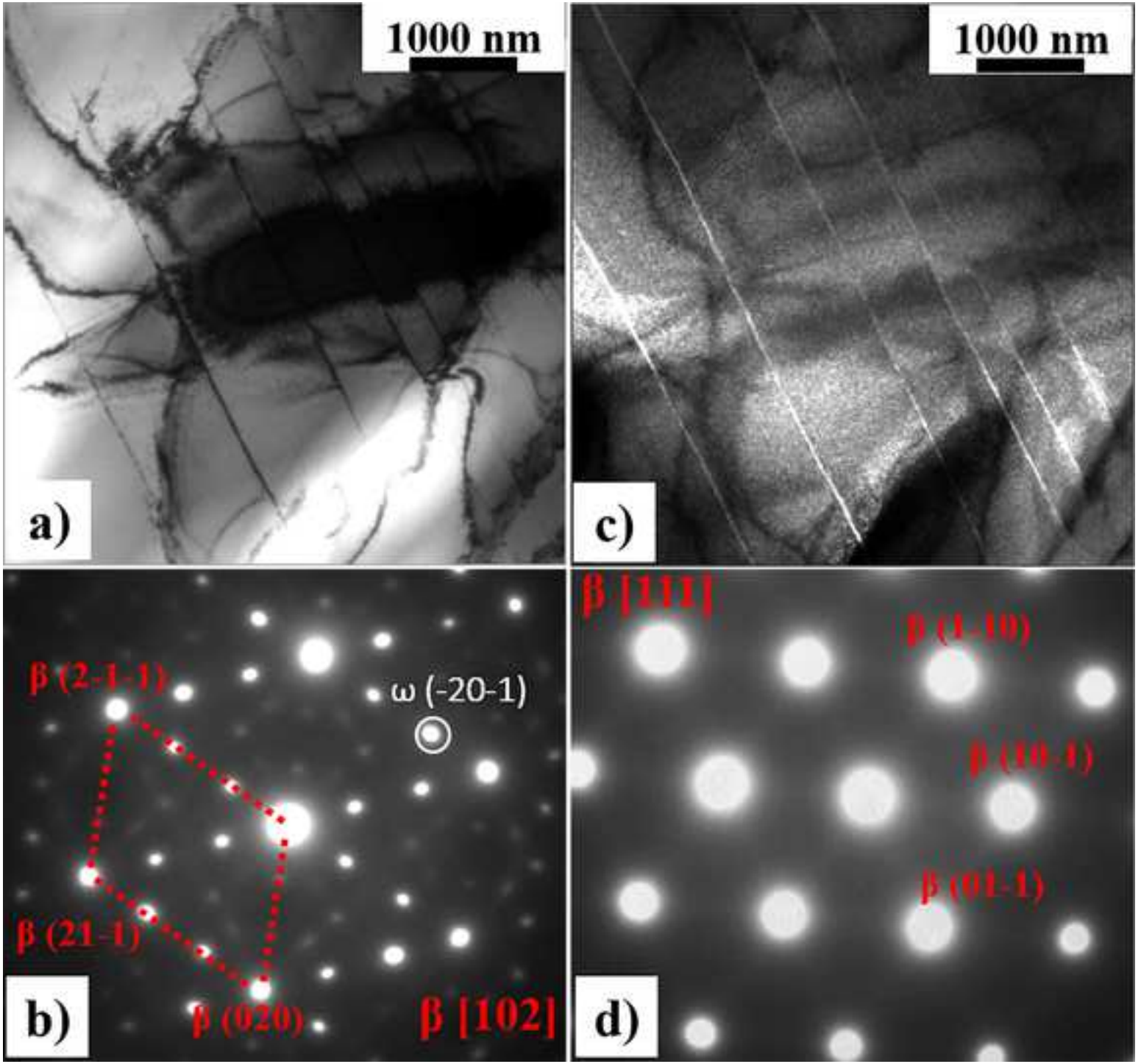

CRediT authorship contribution statement

C.C. Bortolan: Conceptualization, Methodology, Investigation, Writing - review & editing. **L.C. Campanelli:** Investigation, Writing- review. **G. Barucca:** Resources, Investigation, Writing - review. **P. Mengucci:** Resources, Investigation, Writing - review. **N. Giguère:** Methodology, Investigation, Review. **N. Brodusch:** Investigation, Review. **C. Paternoster:** Methodology, Review. **C. Bolfarini:** Supervision, Review. **R. Gauvin:** Resources, Review. **D. Mantovani:** Resources, Funding acquisition, Supervision, Review.

Declaration of interests

☒The authors declare that they have no known competing financial interests or personal relationships that could have appeared to influence the work reported in this paper.

☐The authors declare the following financial interests/personal relationships which may be considered as potential competing interests: